UNIVERSIDAD DE CONCEPCIÓN
FACULTAD DE CIENCIAS FÍSICAS Y MATEMÁTICAS

OPTICAL MODULATION TO ENHANCE EVENT RATE DETECTION BY NEUROMORPHIC CAMERAS IN MICROSCOPY APPLICATIONS

Tesis presentada a la Facultad de Ciencias Físicas y Matemáticas de la Universidad de Concepción para optar al grado académico de Magíster en Ciencias con Mención en Física

Por: José Ignacio Huenchual Escobar

Profesor Guía: Dr. Pablo Solano Palma
Profesor Co-Guía: Dr. Juan Pablo Staforelli Vivanco

Marzo 2025
Concepción, Chile

A mis abuelas, Gladys y María Luisa,
y a mi madre, Margarita

AGRADECIMIENTOS

Este trabajo corresponde al hito final de siete años de estudio en la Universidad de Concepción, años en los que he crecido tanto personal como profesionalmente. Durante este tiempo he sido afortunado de recibir el apoyo de muchas personas, algunas a las que he conocido en este camino y otras que han estado conmigo desde antes. A todas ellas, les agradezco de corazón.

En particular, quiero agradecer a mi madre, Margarita, que me ha apoyado durante tantos años en cada proyecto que he emprendido, incluso cuando puedan parecer un tanto descabellados. Sin tu apoyo y amor incondicional no sé cómo hubiera podido llegar hasta aquí. A mi hermanito, Agustín, que siempre ha estado ahí para sacarme una sonrisa y recordarme que la vida no es solo trabajo. A mi padre, José, por cuidarme a lo largo de todos estos años y apoyarme cuando lo he necesitado. Y a mi familia en general, que siempre ha estado junto a mí en cada paso que he dado y que me inculcaron este interés por la búsqueda del conocimiento.

A mi pareja, Denisse, por su apoyo estos últimos años, por su comprensión cuando el tiempo no alcanza y por sus consejos en los momentos de duda.

Agradezco a quienes me han guiado en la investigación científica durante estos años. A mi profesor guía, Dr. Pablo Solano, por su disposición desde el primer día, su apoyo en distintos proyectos y por la confianza que depositó en mí para llevar a cabo este trabajo. A mi profesor co-guía, Dr. Juan Pablo Staforelli, por haberme recibido en su laboratorio y guiado en el mundo de la óptica.

También agradecer a mis amigos, por su apoyo y compañía durante estos años. Entre ellos, quiero agradecer especialmente a Pedro Contreras, por su compañía en tantas horas de estudio, por ser un gran compañero en proyectos y un amigo en quien siempre puedo confiar, gracias por siempre estar. A Tomás Troncoso, por su constante apoyo, en particular los últimos años en el laboratorio, y por ayudarme a usar los filtros de frecuencia. A Gerardo Millar, por ser un gran compañero de estudio desde el primer semestre, los primeros años hubieran sido mucho más duros sin tu apoyo. A Nicolás Parra, por los cafés y su ayuda al incorporar el

análisis de entropía y complejidad en este trabajo. A Catalina Díaz, por ser una gran amiga por tantos años. Y a Lorena Sepúlveda, por su apoyo estos últimos años, en especial cuando la motivación escaseaba.

Por último, agradecer a la Agencia Nacional de Investigación y Desarrollo (ANID) por financiar parcialmente esta tesis mediante la Beca de Magíster Nacional N°22231084, y a la Universidad de Concepción por haberme otorgado la Beca de Ciencias Físicas y la Beca de Articulación Pregrado-Postgrado. Sin estos aportes, esta tesis no habría sido posible.

Resumen

En esta tesis presentamos una estrategia robusta y no invasiva para optimizar la detección y seguimiento de micropartículas brownianas utilizando cámaras basadas en eventos, inspiradas en estudios sobre visión neuromórfica, mejorando su funcionalidad más allá de la configuración interna del sensor. Mediante la introducción de un movimiento oscilatorio artificial de la imagen en el plano del sensor utilizando un espejo direccionable, incrementamos significativamente la tasa de registro de eventos, mejorando así la resolución espaciotemporal de las partículas rastreadas. A partir de la distribución espacial de los eventos detectados, identificamos de forma efectiva las posiciones de los centros de masa de partículas aisladas sin conocimiento previo de sus formas, superando las limitaciones de los algoritmos de seguimiento basados en centroides de partículas.

En nuestro experimento, empleamos una modulación con una frecuencia de 1 kHz en el plano de imagen, logrando una mejora de hasta 400 veces en la resolución temporal. Para validar nuestro método, caracterizamos el movimiento browniano de una micropartícula midiendo su posición para calcular su varianza y coeficiente de difusión a diferentes temperaturas. Adicionalmente, utilizamos la entropía de permutación como método estadístico para confirmar que nuestra modulación artificial no alteró la naturaleza estocástica de la partícula detectada, asegurando que nuestro enfoque está libre de artefactos.

Keywords – Cámaras basadas en eventos, Movimiento Browniano, Seguimiento de partículas, Mejora de detección

Abstract

In this thesis we present a robust, non-invasive strategy to optimize the detection and tracking of Brownian microparticles using event-based cameras inspired by neuromorphic vision, enhancing their functionality beyond the internal sensor settings. Using a steering mirror, we carried out an optical sway to make an oscillatory motion of the imaging plane on the sensor. This strategy allowed a significant increase in the event recording rate, thereby improving the spatiotemporal resolution to detect the center of mass of tracked particles. From the spatial distribution of detected events, we effectively identify the positions of isolated particles without prior knowledge of their shapes, bypassing the limitations of tracking algorithms based on particle centroids.

In our experiment, we employed a 1 kHz modulation rate of the image plane, achieving up to a 400-fold enhancement in temporal resolution. To test our method, we characterized the Brownian motion of a microparticle by measuring its position to calculate its variance and diffusion coefficient at various temperatures. Additionally, we utilized permutation entropy as a statistical method to confirm that our artificial modulation did not alter the stochastic nature of the detected particle, ensuring our approach is artifact-free.

Keywords – Event-Based Cameras, Brownian motion, Particle tracking, Detection enhancement

Contents

References **59**

List of Tables

List of Figures

Chapter 1

Introduction

Detecting and tracking Brownian microparticles play a vital role in numerous scientific fields exploring the microscale, from physics to biology [1, 2]. The nature of these problems challenges us to detect sub-micron displacements at speeds below milliseconds. Here, efforts are focused on enhancing real-time data acquisition frequencies to overcome the temporal resolution limitations of traditional imaging detectors, such as Complementary Metal-Oxide-Semiconductor (CMOS) or charge-coupled device (CCD) [3].

Inspired by the human visual system, event-based cameras (EBCs) capture changes in light intensity rather than full frames [4, 5]. This asynchronous sensing paradigm offers unique advantages that have not been thoroughly explored in the study of the micro regime. EBCs can detect rapid changes in light intensity with microsecond precision, enabling the tracking of fast particles. Moreover, this new acquisition paradigm allows EBCs to significantly minimize data generation, which reduces computational costs and power consumption. Due to these features, using EBCs for detecting and tracking micro-objects has garnered interest over the past two decades. One pioneering work in this area, by Drazen et al. [6], implements velocimetry of 950 μm microspheres by converting events into frames to be processed with standard imaging particle tracking software. Shortly thereafter, Ni et al. [7] demonstrated the tracking of 12 μm microspheres, detecting Brownian motion by combining the Hough circle transform and centroid method. Additionally, other applications related to fast-tracking or the detection of faint emission sources have been developed in different fields, including electronic

microscopy, single-molecule localization microscopy, and stereo velocimetry for 3D object reconstructions [8–16]. However, none of these efforts have focused on improving event statistics through optical techniques that do not depend on the nature of the object of interest.

Imaging sensors can be classified into two categories: classical sensors that rely on image intensity acquisition and non-classical sensors that focus on event capture. Classical sensors may differ in their acquisition architecture. For example, in CMOS technology, pixel acquisition occurs sequentially, resulting in issues such as the rolling shutter effect, which causes images of objects to appear stretched or incomplete. This problem is closely associated with the data acquisition speed and streaming capacity. As a result, CCD sensors are used to address this challenge due to their parallel architecture for pixel data transmission. Nevertheless, both classical sensors share an essential characteristic: they rely on continuous data streaming defined by the frames per second (FPS), and the only method to increase streaming speed is to reduce the region of interest (ROI). For faster acquisition, decreasing the ROI limits the number of pixels an object can occupy in the image, restricting the sampling of its shape and, ultimately, the spatial resolution. This limitation is evident when tracking a particle using the centroid method; increasing the number of pixels occupied by the particle reduces the statistical error in estimating its centroid, albeit at the cost of lower temporal sampling. Refer to Fig. 1.0.1 for a visual representation of this issue.

In contrast, the second category changes this paradigm. The images are replaced by events associated with the activation of logical pixel values due to variations in brightness. For instance, the motion of an object alters the light intensity in the image plane at the camera sensor, thus recording events in multiple pixels depending on the shape of the object and its direction of motion. A key difference between EBCs and classical ones is that the acquisition frequency for this type of sensor, usually around 1 MHz, is unaffected by the ROI. A major challenge when using EBCs to observe a specific phenomenon, such as a moving particle, is capturing enough events related to that motion. A larger number of events in the image provide more data for accurately determining the centroid of the object without sacrificing image size or acquisition speed, while a faster rate of events reduces the time between acquisitions thus improving the temporal resolution. A combination of large number and fast rate of events leads to a larger stream of

events that translates into an improved spatiotemporal resolution of the observed object as shown in Fig. 1.0.1.

The performance of EBC varies based on the diversity of scene motion and the intensity of background-object contrast, among other factors. This requires minimizing background noise while maximizing events associated with the observed moving object. Systems that generate few events limit the potential of EBC. To address this, event generation must be increased, typically by modifying the sample or adjusting camera bias values. However, increasing events without impacting the physical phenomenon is challenging. For instance, changing the temperature of the sample or utilizing dyed particles can enhance motion diversity and contrast but may denature live specimens. Indirect methods, such as variable illumination, can influence self-propelled particles that depend on phototaxis dynamics, as observed in certain bacteria and micro-algae, or on photo-catalytic propellants, as seen in Janus micro-particles [17], affecting both the background and the object. Furthermore, raising the bias threshold further amplifies noise.

This work proposes a method to increase the event stream while avoiding these issues. We introduce a controlled relative motion between the camera and the image plane, which can be applied just before the light reaches the EBC, ensuring that the observed object dynamics remain unchanged. Such motion is introduced into the system by a piezoelectric-controlled steering mirror. We characterize the Brownian motion of a spherical microparticle suspended in water as a testbed for our method. We can isolate the particle movement by leveraging background homogeneity in the image. This strategy enables us to controllably increase the streaming of events, thereby improving both the temporal resolution and the event counting statistics for accurate estimation of the center of the particle. We validate our technique by measuring relevant physical parameters, such as the diffusion coefficient, and performing statistical analysis of the motion, ensuring the method is artifact-free.

The main objective of this research, and the central topic for this thesis, is to develop and validate a nobel methodology to improve the performance of event-based cameras in microscopy, in particular for microparticle tracking applications. This general aim is addressed through three specific objectives: (1) to implement an experimental setup with the capability to introduce the controlled relative motion between the camera and the image plane as is proposed in this work, (2) to

develop an algorithm to convert the resulting event stream into particle trajectories and (3) to validate the proposed method by measuring temperature-dependent Brownian motion parameters and verifying the preservation of the stochastic nature of the particle motion through entropy-based analysis.

This thesis is organized as follows: Chapter 2 provides the theoretical framework, covering the fundamentals of event-based cameras, Brownian motion physics, frequency filtering techniques, and the mathematical foundations of permutation entropy and statistical complexity. Chapter 3 presents a detailed description of the experimental methodology, including the optical setup, detection methods, and comprehensive data processing protocols, including different approaches to obtain the diffusion coefficient from the particle trajectories. Chapter 4 analyzes the experimental results. Finally, Chapter 5 presents the conclusions and perspectives of this work.

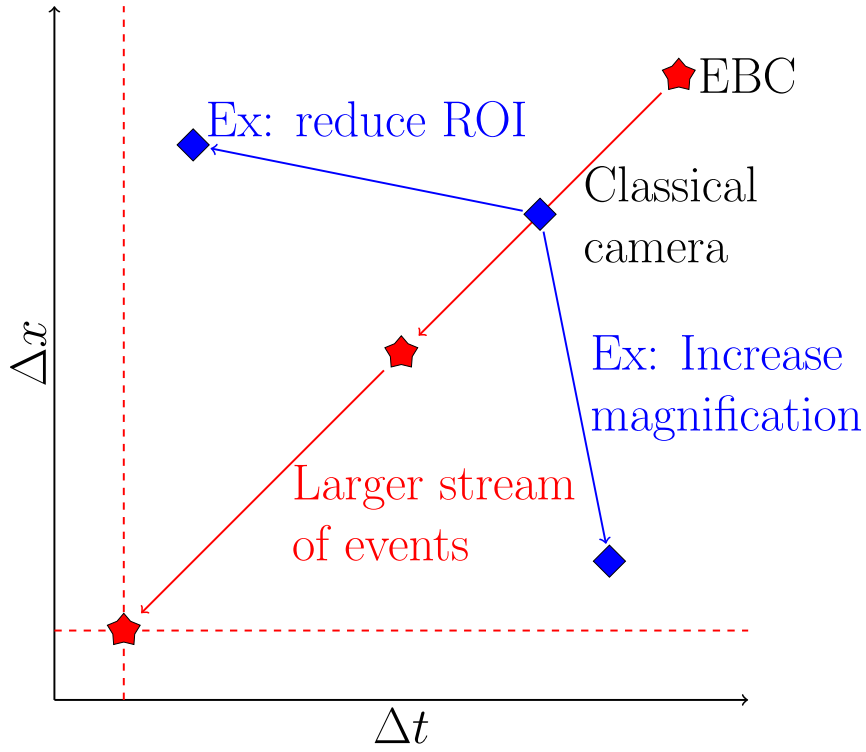

Figure 1.0.1: Comparison of temporal (Δt) and spatial (Δx) resolution for classical and event-based cameras. Classical cameras acquire images with a fixed number of pixels that refresh simultaneously to form a frame. The ROI size generally determines their acquisition frequency, while the pixel-to-length ratio defines their spatial resolution. In contrast, the acquisition frequency of event-based cameras is independent of the ROI, allowing for a high acquisition rate regardless of sensor size. However, the number of detected events limits the ability to identify an object and its position, and increasing the time window to accumulate more events reduces the acquisition rate. This means that the sample, not the camera, constrains the spatiotemporal resolution. A larger stream of events improves both temporal and spatial resolution to reach the optimal acquisition rate and pixel size of the hardware (red dashed line).

Chapter 2

Theoretical Framework

This chapter presents the theoretical foundations necessary to understand the methods and results discussed in this thesis. We begin by exploring the principles and capabilities of event-based cameras, the technology at the core of our study. Following this, we review some key mathematical relations for Brownian motion, particularly on the mean square displacement and it's relation with diffusion coefficient calculations. We then address some details for frequency filtering, centered in a particular type, the Butterworth filters. Finally, we introduce the definitions of permutation entropy and statistical complexity, values that serve as tools to validate our proposed methodology.

2.1 Event-based sensors and cameras

Event-based sensors represent a paradigm shift in vision sensing technology, moving away from the frame-based approach. Inspired by biological vision systems, hence their relation with neuromorphic vision, these sensors operate on fundamentally different principles that prioritize temporal precision and sensibility. The concept was first introduced by Mahowald and Mead with their pioneering work on the silicon retina [4], which laid the groundwork for modern event-based cameras (EBCs). Unlike conventional cameras that capture entire frames at fixed time intervals regardless of scene content, each pixel of an EBC operates independently, making of the whole device an example of asynchronous detection. This novel approach to visual sensing result in a camera with a high temporal resolution, high dynamic range, high pixel bandwidth, low power consumption, and reduced

data rate [5]. This makes EBCs particularly well-suited for tracking fast-moving objects like Brownian microparticles.

2.1.1 What is the working principle?

The fundamental principle behind event-based sensors is the detection of local changes in luminance rather than absolute light intensity, and recording them as they occur instead that a fixed temporal rate. Each pixel in an event-based camera operates independently and asynchronously, continuously monitoring the logarithm of the intensity (log intensity) of the light that is detected at said pixel. When the change in log intensity exceeds a predefined threshold, the pixel generates an "event". This approach is related to biological systems and neuromorphic technology, as work on the principle that : “Biological vision systems are driven and controlled by events happening within the scene in view, and not, like image sensors, by artificially created timing and control signals that have no relation whatsoever to the source of the visual information and its dynamics.” as stated by Posch et al. [18]. In particular, they are related to the principle of how certain elements of vision systems, known as transient visual pathways, work. More details on this can be found at section 3.3 of the article of Gallego et al. [5].

The pixel circuit in an event-based camera typically consists of a photodiode that converts light into electrical current, followed by a logarithmic compression stage that mimics the adaptive response of biological photoreceptors. After logarithmic conversion, a differencing circuit compares the current log intensity with the previously stored value. When the difference exceeds the threshold (either positively or negatively), the pixel triggers an event and updates its stored reference value. The real circuit behind this process is more complex, and one example of it is known as the Dynamic Vision Sensor (DVS) that is described in detail by Lichtsteiner et al. [19].

2.1.2 How is the data stored?

Each generated event contains four pieces of information, as illustrated in Figure 2.1.1: the spatial coordinates of the pixel (x, y), the precise timestamp of the change (t) usually with microsecond resolution, and the polarity (p) indicating whether the brightness increased (+1) or decreased (-1). This creates a sparse, asynchronous stream of events representing the visual information in the scene.

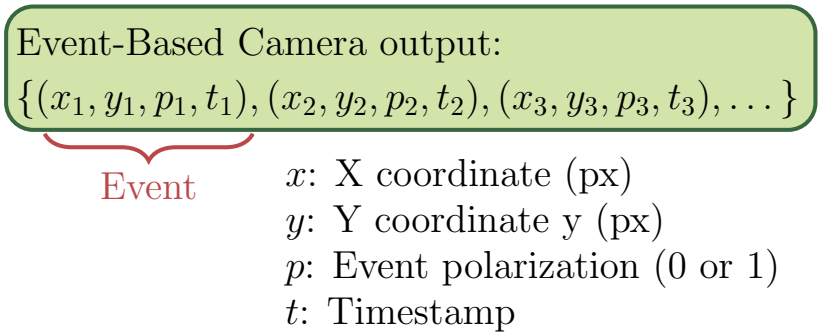

Figure 2.1.1: Event storage format. This is a diagram of the event storage format in a EBC. Each event detected is stored as a tuple containing four values as showed, the continuous detection of events result in a list of these tuples.

As EBCs are data-driven sensors the amount of events generated and the memory used to store them is directly related to the amount of motion or brightness change in the scene. The faster the motion, the more events per second are generated. Due to this they need to be stored sequentially in a data structure often referred to as an "event stream" or asynchronous address representation" (AER).

For analysis, visualization, and processing purposes, the raw event stream can be converted into various representations, including:

- Time surfaces: 2D maps where each pixel value represents the timestamp of the most recent event at that location
- Event frames: Accumulations of events over specific time windows to create frame-like representations
- Voxel grids: 3D volumes where events are binned in both space and time

2.1.3 What are the advantages over conventional cameras?

Event-based cameras offer several significant advantages over conventional frame-based cameras, particularly for applications involving fast-moving objects and scenes with localized or sparse motion [5, 7]:

- **High temporal resolution:** Event-based cameras can achieve temporal resolutions on the order of microseconds, allowing for the capture of extremely rapid phenomena.
- **High dynamic range:** Event-based sensors can achieve dynamic ranges

exceeding 120 dB, compared to 60-70 dB for conventional cameras. This allows them to operate effectively in scenes with both very bright and very dark regions simultaneously.

- **Lower power consumption:** The sparse, change-driven nature of event generation results in significantly reduced power consumption compared to conventional cameras, making event-based sensors particularly suitable for battery-powered or energy-constrained applications.
- **Reduced data rate:** By capturing only changes in the scene rather than complete frames, event-based cameras generate significantly less data than conventional cameras, particularly in scenes with limited or localized motion. This reduces bandwidth requirements for data transmission and storage, as well as computational load for subsequent processing.

To exemplify the reduced data rate, and how this affects the storage requirements, consider a one-minute video captured by a conventional camera with the following specifications:

- Resolution: 640×480 pixels
- Frame rate: 20,000 fps
- Color depth: 8-bit grayscale (values from 0 to 255)
- Duration: 60 seconds

Each pixel requires 8 bits (1 byte) for grayscale, considering that the total pixels per frame are $640 \times 480 = 307200$ pixels, the storage required per frame is $307,200$ bytes or approximately 300 KB. And the whole video would require 300 KB/frame $\times 20,000$ fps $\times 60$ seconds = 360 GB of storage.

Therefore, you would need approximately 344 GB of storage space for a one-minute grayscale video with these specifications, assuming uncompressed storage with no overhead. In contrast, the EBCs data used for this thesis is composed by several recordings stored in less than 27 GB, from which 37 minutes were used after filtering.

Despite these advantages, event-based cameras also present certain challenges. The asynchronous nature of the data requires specialized algorithms for processing and analysis, different from those developed for conventional frame-based imagery.

Additionally, the contrast sensitivity threshold means that very gradual changes might not generate events, potentially missing some subtle visual information, and this cannot be tackled only by lowering the threshold as eventually noise driven events will dominate the scene. For microparticle tracking applications, as addressed in this thesis, specialized techniques may be needed to enhance event generation in scenarios with insufficient natural motion or contrast.

2.2 Brownian motion

Brownian motion refers to the random movement of microscopic particles suspended in a fluid, resulting from their constant collisions with the molecules in the fluid. This phenomenon was first observed by botanist Robert Brown in 1827, hence the name, while examining pollen grains suspended in water under a microscope [20]. However, the theoretical foundation explaining this movement was not established until the early 20th century, when Albert Einstein [21] and, independently, William Sutherland [22] developed mathematical models connecting these observable random movements to the molecular structure of matter.

Einstein's approach was particularly significant as it established a quantitative relationship between the observable displacement of particles and molecular dimensions. The particular elements from his work that are relevant to this works are the demonstration that the mean square displacement of Brownian particles increases linearly with time, with the proportionality constant (the diffusion coefficient) determined by fundamental physical parameters including temperature, fluid viscosity, and particle size.

In our research, Brownian motion serves both as the phenomenon under observation and as a validation tool. By tracking the random movement of microparticles in a fluid using event-based cameras, we can assess whether our detection and tracking methodology preserves the statistical characteristics of the motion while enhancing detection capabilities. The mathematical framework developed for Brownian motion provides us with well-established analytical tools to verify our experimental results against theoretical predictions.

2.2.1 Mean square displacement (MSD) and Diffusion coefficient

The mean square displacement (MSD) is a fundamental measure used to characterize random motion processes such as Brownian motion. It quantifies how far a particle travels from its starting position over a certain time window, averaged over many observations or particles or the same particle at different instances.

For a particle trajectory represented by position vectors $\vec{r}_i = (x_i, y_i)$, for $i = 1, \ldots, N$ recorded at regular time intervals Δt, the displacement between any two positions is defined as $\Delta\vec{r}_{ij} = \vec{r}_j - \vec{r}_i$, corresponding to a time interval $\tau = (j-i)\Delta t$. The MSD for a given time interval $\tau = n\Delta t$ is then calculated as:

$$\mathrm{MSD}_{2\mathrm{D}}(\tau) = \frac{1}{N-n}\sum_{i=1}^{N-n} |\vec{r}_{i+n} - \vec{r}_i|^2 \ , \tag{2.2.1}$$

and, in a similar way, the MSD in one dimension is given by:

$$\mathrm{MSD}_{1\mathrm{D}}(\tau) = \frac{1}{N-n}\sum_{i=1}^{N-n} (r_{i+n} - r_i)^2 \ . \tag{2.2.2}$$

Einstein's theory of Brownian motion established a direct relationship between the MSD value and the time window for the movement [21], expressed as:

$$\mathrm{MSD}_{1\mathrm{D}}(\tau) = 2D\tau, \tag{2.2.3}$$

$$\mathrm{MSD}_{2\mathrm{D}}(\tau) = \mathrm{MSD}_{1\mathrm{D},x}(\tau) + \mathrm{MSD}_{1\mathrm{D},y}(\tau) \tag{2.2.4}$$

$$= 4D\tau, \tag{2.2.5}$$

$$\mathrm{MSD}_{3\mathrm{D}}(\tau) = 6D\tau, \tag{2.2.6}$$

where D is the diffusion coefficient of the particle in the medium. In practice, when working with experimental position data, we observe that $\mathrm{MSD}(\tau = 0) = \epsilon > 0$, where ϵ is related to the localization error of the measurement system, this relation is explored in detail at the work of Michalet et al. [23]. This offset must be accounted for when fitting experimental data to extract the diffusion coefficient.

It's important to note that in our experimental setup, the measured particle

position combines true Brownian motion with a superimposed sinusoidal displacement caused by our optical modulation method using a steering mirror. This additional motion introduces a periodic component to the MSD curve that can obscure its linear behavior. This challenge will be addressed at the section 3.5.

2.2.2 Stokes-Einstein-Sutherland equation

For spherical particles suspended in a fluid, as is our case of interest, the diffusion coefficient can be related to fundamental physical parameters through the Stokes-Einstein-Sutherland equation:

$$D = \frac{\kappa_B T}{6\pi\eta R}, \tag{2.2.7}$$

where κ_B is the Boltzmann constant (1.380649×10^{-23} J/K), T is the absolute temperature in Kelvin, η is the dynamic viscosity of the fluid, and R is the radius of the particle [21, 22].

This equation establishes a direct relationship between the observable diffusion coefficient and microscopic properties of the system. It predicts that the diffusion coefficient increases linearly with temperature, decreases inversely with fluid viscosity, and decreases inversely with particle size. These dependencies provide a powerful way to validate our experimental measurements against theoretical expectations.

Figure 2.2.1 illustrates the theoretical diffusion coefficient as a function of temperature for microparticles of different sizes in water, these sizes were chosen by being similar to the ones used in our experiments. The nonlinear increase with temperature results from two opposing factors: the direct proportionality with absolute temperature and the inverse proportionality with viscosity that has a nonlinear relation with temperature, as detailed in the next section.

2.2.3 Dynamic viscosity of water

Among all the parameters that determine D, η is the only one we do not measure directly. Instead, we determine its value and temperature dependence from the literature [24–26]. Additionally, these computed values are cross-verified

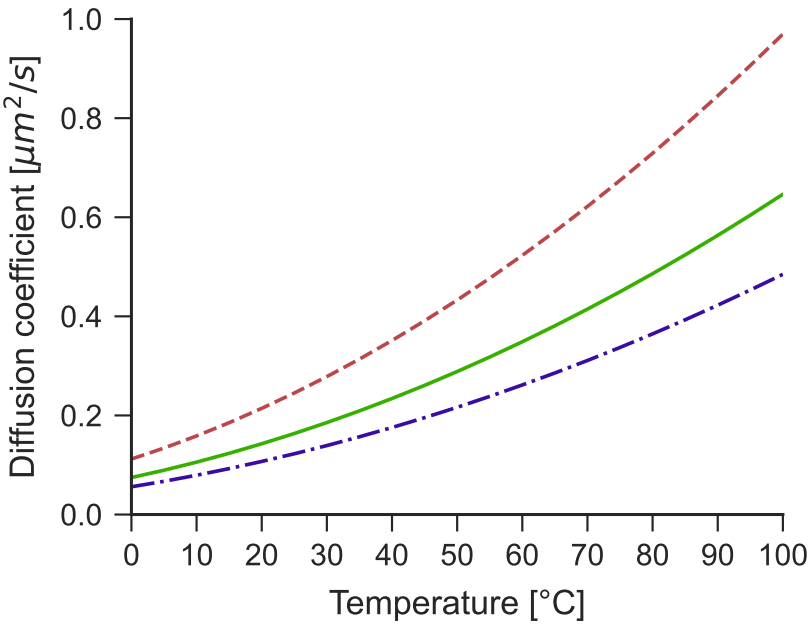

Figure 2.2.1: Diffusion coefficient as a function of temperature for a microparticle in water. Temperature ranges from 0 to 100°C, and for the radius of the particle, we consider $R = 1.0\mu$m (red dashed line), $R = 1.5\mu$m (green solid line), and $R = 2.0\mu$m (blue dashdotted line).

with tables found in a fluid handbook [27] and technical guidelines from The International Association for the Properties of Water and Steam [28, 29]. In general, the dynamic viscosity of substances is calculated using a wide variety of mathematical relations heavily based on empirical data, and the ones used for water are no exception.

The equations used to calculate the dynamic viscosity of water (in kg/m·s) as a function of temperature were obtained from the CRC Handbook of Chemistry and Physics, 69th edition [24]. Said equations are:

$$\eta_{\text{water}}(T) = \begin{cases} 10^{-3}(10^{A(T)}), & \text{for } 0 < T < 20°\text{C} \\ 1.002 \cdot 10^{-3}(10^{B(T)}), & \text{for } 20 < T < 100°\text{C} \end{cases} \tag{2.2.8}$$

where,

$$A(T) = \frac{1301}{a + b(T-20) + c(T-20)^2} - 1.30223,$$
$$B(T) = \frac{1.3272(20-T) - 0.001053(T-20)^2}{T + 105},$$

with constants $a = 998.333$, $b = 8.1855$, and $c = 0.00585$.

The expression for viscosity below 20°C comes from the work of Hardy and Cottington [25], while the one for temperatures above 20°C was proposed by Swindells et al. [26].

Table 2.2.1 presents calculated values of for the dynamic viscosity of water. using these equations, across the whole range of temperatures for which temperature is liquid at atmospheric pressure, 0°C to 100°C. The strong temperature dependence of viscosity is evident, with the value decreasing by more than 80% from freezing to boiling point.

Temp. [°C]	0	10	20	30	40	50
η	1.787	1.307	1.002	0.798	0.653	0.547
Temp. [°C]	60	70	80	90	100	-
η	0.467	0.404	0.355	0.315	0.282	-

Table 2.2.1: Dynamic viscosity values for pure water in the range of 0 to 100°C. They were calculated using the equations presented in the text.

2.3 Butterworth frequency filters

Frequency filtering is an essential signal processing technique that allows selective attenuation or amplification of specific frequency components within a signal. In our experimental analysis, we employ frequency filters to separate the Brownian motion component from the periodic effect of our optical modulation. The relevance of this step goes beyond the calculation of the diffusion coefficient, as in the ideal situation of having a technique to perfectly separate them we could use any traditional method to analyze the trajectories of the particles, without needing special considerations for the optical modulation.

Linear frequency filters can be broadly categorized into several types based on their response characteristics. These including, but not limited to, Butterworth, Chebyshev (Types I and II), and elliptic filters, which differ primarily in how they manage the transition from passband to stopband, as illustrated in Figure 2.3.1:

- **Butterworth filters**, introduced by physicist Stephen Butterworth in 1930 [30], provide maximally flat frequency response in the passband with no ripple, though they sacrifice steepness in the transition.

- **Chebyshev Type I filters** offer steeper transition than Butterworth filters but introduce ripple in the passband.
- **Chebyshev Type II filters** maintain a flat passband but introduce ripple in the stopband, the inverse of what occurs with the type I.
- **Elliptic filters** provide the steepest transition but exhibit ripple at both sides.

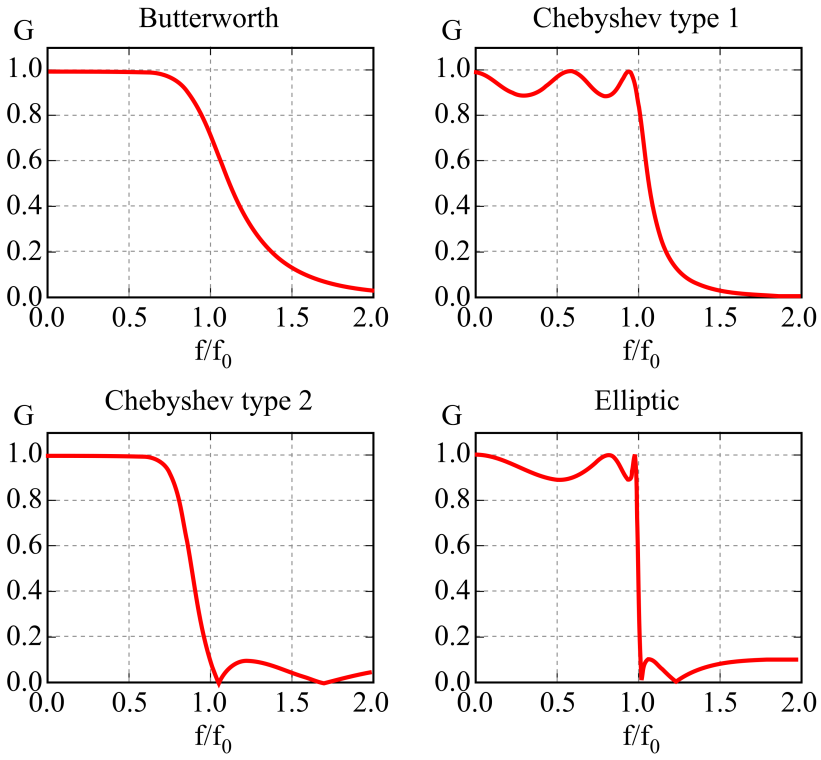

Figure 2.3.1: Comparison in the frequency response of different types of low-pass filters. The filters shown are Butterworth, Chebyshev type I, Chebyshev type II, and elliptic filters, all of 5th order. With gain normalized and frequency measured as multiples of the break frequency. Figure taken from Wikimedia Commons [31], licensed under CC BY 4.0.

Each filter type can be implemented in four fundamental configurations:

- **Low-pass filters** allow signals below a cutoff frequency to pass while attenuating higher frequencies.
- **High-pass filters** allow signals above a cutoff frequency to pass while attenuating lower frequencies.
- **Band-pass filters** allow signals within a specified frequency range to pass

while attenuating those outside this range.

- **Band-stop filters** attenuate signals within a specified frequency range while allowing those outside this range to pass.

In our work, we specifically employ band-stop Butterworth filters to selectively remove the frequency components associated with our optical modulation, with the idea of preserving the characteristics of the underlying Brownian motion.

A key parameter affecting filter performance is the filter order, which determines the steepness of the transition between passband and stopband. As shown in Figure 2.3.2, higher-order filters provide sharper transitions but come with increased computational complexity and potential phase distortion. For a Butterworth filter, the magnitude response is given by:

$$|H(\omega)|^2 = \frac{1}{1 + \left(\frac{\omega}{\omega_c}\right)^{2n}} \tag{2.3.1}$$

where ω is the angular frequency, ω_c is the cutoff frequency, and n is the filter order. The rate at which the magnitude response drops in the transition band is approximately $20n$ dB/decade, where a "decade" means a 10x change in frequency

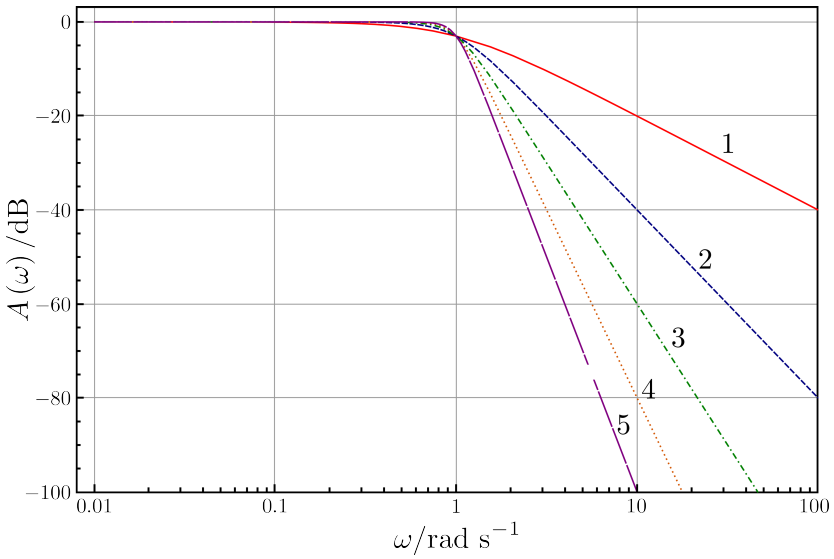

Figure 2.3.2: Frequency response of a low-pass Butterworth filter at different orders. Orders from 1st to 5th are shown, with the break frequency normalized to 1 rad/s and the gain normalized to 0 dB. Figure created by Inductiveload and taken from Wikimedia Commons [32]. This figure is in the public domain.

The frequency response for a butterworth band-stop filter looks like a valley. In the figure 2.3.3 three filters with different orders are shown (4th, 8th, and 16t), all centered at 1 kHz with a bandwidth of 200 Hz. Here we can observe that higher-order filters create narrower transition regions and deeper valleys, effectively isolating and removing targeted frequency components. To target an specific frequency, would be desirable to use a high order filter, but this can lead to distortions in the signal, so the selection of the order is a trade-off between these two factors.

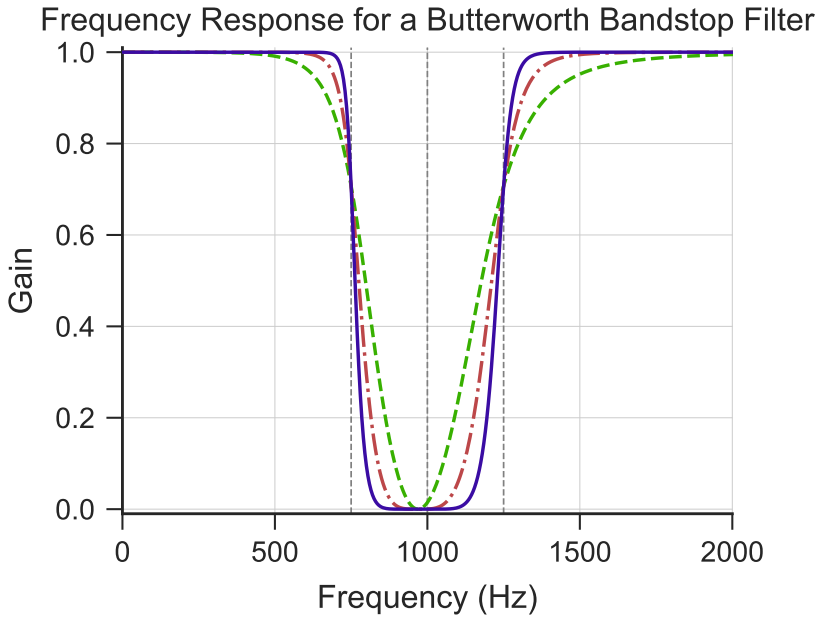

Figure 2.3.3: Frequency response of a Butterworth bandstop filter. The filter is centered at 1 kHz with a bandwidth of 250 Hz, and three different orders are shown: 2th (dashed), 4th (dashdotted) and 8th (solid) order.

In our application, these band-stop filters allow us to precisely filter out the modulation frequencies from our trajectories while minimizing the impact on the surrounding frequency components that contain information about the Brownian motion dynamics.

2.4 Permutation entropy and Statistical complexity

Due that the proposed method for externally increasing the number of events relies on modulating the image plane, one might think the modification of the

stream of events in the EBC could alter the dynamics and statistics of the tracked microparticle. To prove that this is not the case, we employ mathematical tools from information theory. Specifically, permutation entropy and statistical complexity serve, they serve as quantitative measures to characterize time series dynamics, allowing us to distinguish between random and deterministic behaviors.

The calculations of these quantities were done using the python package `ordpy` [33], which provides an efficient implementation of permutation entropy and statistical complexity calculations. Their article presenting the package is one of the main references for this section.

2.4.1 Permutation entropy

Permutation entropy (PE) is a mathematical tool for quantifying the randomness of a time series [34]. It is useful for analyzing nonlinear and noisy data, making it suitable for various fields, including biology, finance, and micro-physics [35–40]. The key advantages of PE include its robustness to noise, and computational efficiency.

The calculation of PE involves several steps, steps 1 and 2 are illustrated at figure 2.4.1:

1. First, the time series is divided into segments of length m (the embedding dimension), where each segment consists of m consecutive data points.

2. Within each segment to each number is given an index representing their original position in the segment, then the values are ranked from smallest to largest, and their index create what is called an ordinal pattern. This represents the relative ordering of values rather than their absolute magnitudes. Each ordinal pattern corresponds to one of the $m!$ possible permutations.

3. The frequency of each ordinal pattern is determined across all segments in the time series, generating a probability distribution $P = \{p(\Pi_i)\}$, where $p(\Pi_i)$ is the probability of observing the ordinal pattern Π_i.

4. Finally, Shannon entropy is calculated based on this probability distribution,

$$S(P) = -\sum_{i=1}^{m!} p(\Pi_i) \log p(\Pi_i) \,. \tag{2.4.1}$$

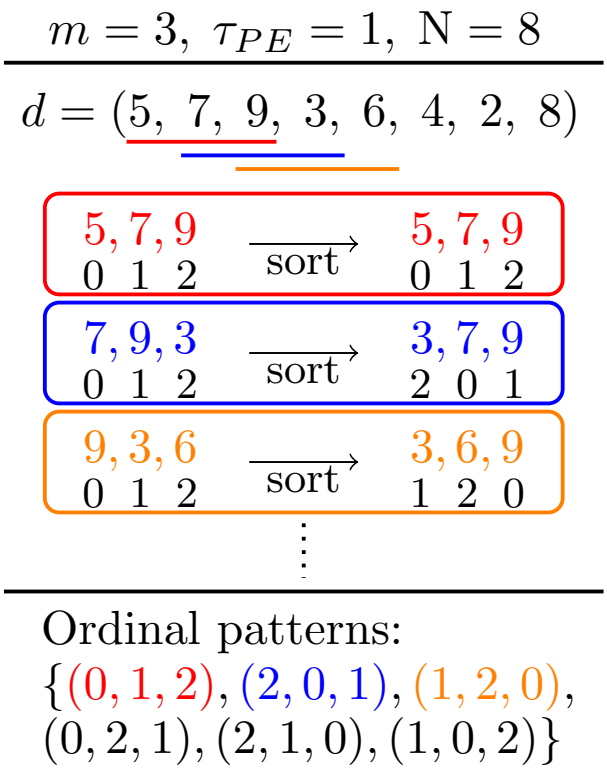

Figure 2.4.1: Ordinal pattern identification from a dataset. This diagram represents how to obtain the ordinal patterns from a dataset using an embedding dimension equal to 3.

The normalized permutation entropy is defined as,

$$H(P) = \frac{S(P)}{\log(m!)}\,. \tag{2.4.2}$$

This normalization constrains the PE value between 0 and 1, where values closer to 1 indicate more random or complex behavior, while values closer to 0 suggest more predictable or regular patterns [33].

When applying PE to analyze time series, two key parameters must be carefully selected:

1. The embedding dimension m, which determines the length of the patterns and the number of possible permutations ($m!$). Following the recommendation from Bandt and Pompe [34], later refined by Cuesta-Frau et al. [41], it is common to choose values of m such that $m! \ll N$ where N is the length of the series to obtain reliable PE values.

2. The embedding delay τ_{PE}, which defines the time separation between consecutive points within each pattern. The value for embedding delay varies depending on the application, but for calculations on Brownian motion, it is common to use a value of $\tau_{PE} = 1$ [42].

2.4.2 Statistical complexity

While permutation entropy quantifies the degree of randomness in a time series, it does not fully capture the structural complexity that distinguishes different types of dynamics. To address this limitation, the statistical complexity (SC) measure provides complementary information by quantifying the balance between disorder (entropy) and structure. This approach is particularly valuable for analyzing systems that are neither entirely random nor entirely deterministic, as is the case in our experimental setup, where Brownian motion coexists with periodic optical modulation.

The statistical complexity measure we employ is based on the Jensen-Shannon complexity proposed by Rosso et al. [43], which builds upon the earlier work of López-Ruiz et al. [44]. The measure is defined as:

$$C(P) = D(U, P) \cdot H(P)/D_{max} \tag{2.4.3}$$

where:

- $H[P]$ is the normalized permutation entropy of the ordinal pattern distribution P.
- $D(U, P)$ is the Jensen-Shannon divergence between P and the uniform distribution $U = \{1/(m!)\}_{i=1,\ldots,m!}$.
- D_{max} is a normalization constant that depends on the number of total permutations.

The Jensen-Shannon divergence is calculated as,

$$D(P, U) = S[(P + U)/2] - (S[P] + S[U])/2, \tag{2.4.4}$$

and, the normalization constant is given by,

$$D_{max} = -\frac{1}{2}\left(\frac{n_\pi! + 1}{n_\pi!}\log(n_\pi! + 1) - 2\log(2 \cdot n_\pi!) + \log n_\pi!\right), \tag{2.4.5}$$

where $n_\pi = m!$ is the number of possible permutations.

This formulation ensures that the complexity measure reaches its maximum value for distributions that are neither completely random nor completely ordered.

2.4.3 Complexity-Entropy plane

The joint analysis of permutation entropy and statistical complexity provides a powerful tool for characterizing different types of dynamics. By plotting these two measures against each other in what is known as the complexity-entropy plane, we can visually distinguish between different types of processes. For example:

- Completely random processes (white noise) are located in the lower-right region, with high entropy and moderate complexity.
- Deterministic processes tend to occupy the left region, with lower entropy and varying complexity.
- Fractional Brownian motion (fBm) with different Hurst exponents forms a distinctive curve in the plane. The Hurst exponent is a measure of long-range dependence in time series, with values between 0.5 and 1 indicating persistent behavior, and values between 0 and 0.5 indicating anti-persistent behavior.

fBm is mentioned because is a mathematical model that generally describes the motion of Brownian particles and its PE values have been well studied [46, 47], this makes it a good reference to compare the results of our experiments.

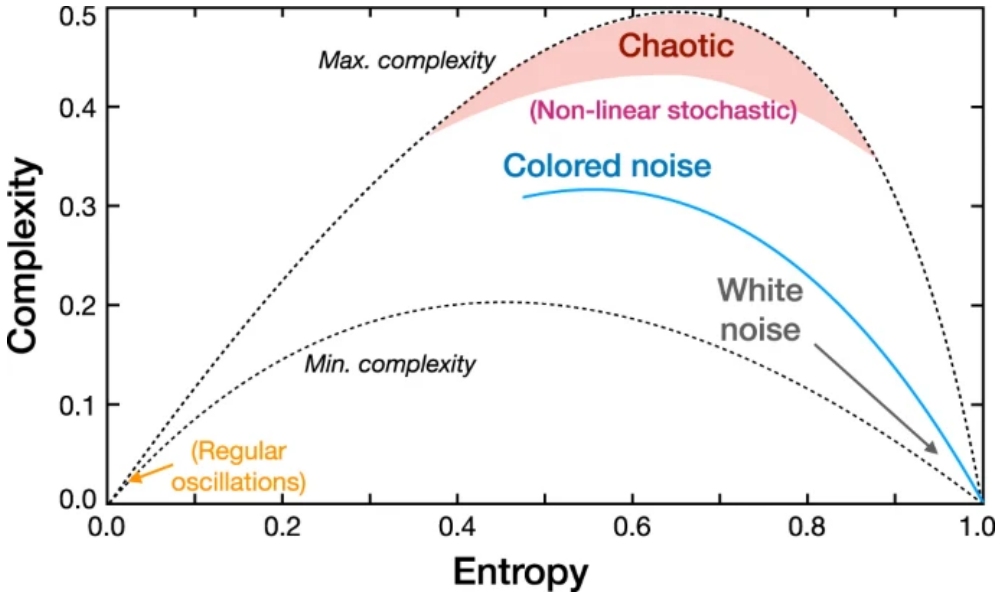

Figure 2.4.2: Complexity-Entropy plane. The plot displays how different regions are related to different types of processes. The solid black lines represent the boundaries for any process at the plane. Figure taken from Ref. [45], licensed under CC BY 4.0.

Chapter 3

Methodology

This chapter details the experimental methodology developed to apply the proposed approach to enhance event detection rates in Brownian microparticle tracking using event-based cameras (EBCs). We begin by describing the experimental setup. Following this, we explain the calibration procedures for spatial resolution and particle size measurement. We then present our method for increasing event detection rates through controlled optical modulation, and detail the algorithms used for particle identification and tracking. The chapter continues with a thorough explanation of our approaches to extract and validate the diffusion coefficient from the acquired trajectories, addressing the challenges posed by the superimposed modulation signal. And finally, we discuss how permutation entropy and statistical complexity are calculated from our data.

3.1 Experimental setup

Figure 3.1.1 shows a schematic of the optical setup build to test the proposed method. This system is placed on an optical bench (1.5 × 2 m, Thorlabs) for active mechanical isolation. We use a confocal microscope (Eclipse TE-2000U, Nikon) to observe polystyrene microparticles with a diameter of 3 μm (n = 1.59, Kisker-Biothec). The sample used for the experiment correspond to microparticles suspended in a solution of deionized water and sodium dodecyl sulfate (SDS) to prevent aggregation. To preserve the integrity of the solution, a drop of around 10 mul is placed between two standard glass coverslip, with a nominal thickness of 0.13 to 0.17 mm, a 24× 50 mm one serves as the bottom and a 20×20 mm as the

top. Then they are sealed with colorless nail polish to isolate the solution, this prevent evaporation, which is especially important when heating the sample. We implemented Kohler illumination to ensure a uniformly illuminated bright field of view. The image is formed from light transmitted through an x100 objective lens (MRD01991, Nikon), achieving a pixel-to-spatial resolution of 51.0 nm/pixel, measured with a micro-calibration test target (USAF 1951, Thorlabs). We use a 1280x124 CMOS sensor camera (DCC1645C-HQ, Thorlabs) to optically inspect the sample, identifying, counting, and measuring the radii of the microparticles.

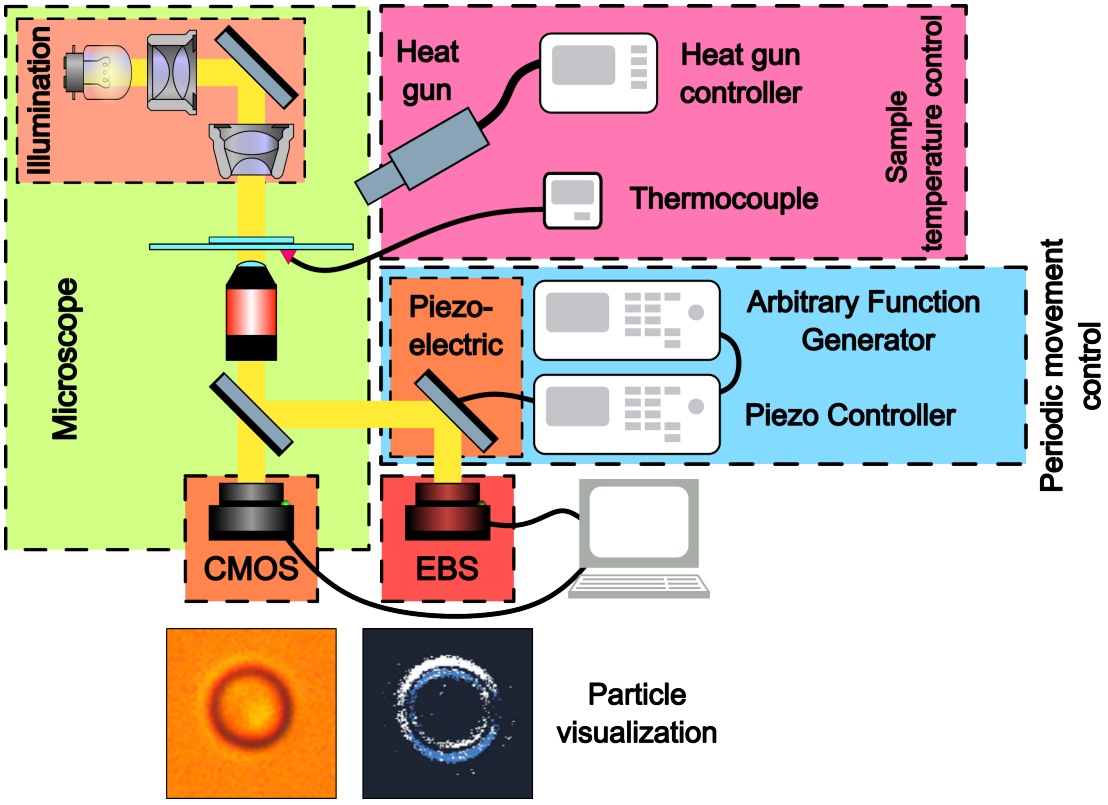

Figure 3.1.1: Optical system implemented to enhance the event acquisition rate in EBS-based microtracking. It comprises three stages. The first stage (green) includes a microscope setup with a visible light source illuminating a microsphere sample, a 100x objective lens with a numerical aperture of 1.4, and a beam splitter that directs light toward both an observation port and a piezoelectric mirror (PZM). The second stage (pink) provides precise temperature control for the sample and consists of a heat gun, a controller, and a thermocouple. The third stage (cyan) controls the motion by utilizing a PZM to create periodic sample movements on EBS, thereby increasing the event generation rate. The PZM is controlled by a piezo-controller connected to an arbitrary function generator.

Figure 3.1.1 shows a schematic of the optical setup build to test the proposed method. This system is placed on an optical bench (1.5 × 2 m, Thorlabs) for

active mechanical isolation. We use a confocal microscope (Eclipse TE-2000U, Nikon) to observe polystyrene microparticles with a diameter of 3 μm (n = 1.59, Kisker-Biothec). The sample holder consists of standard number-0, 0.13 to 0.17 mm thick, glass coverslip sealed with colorless nail polish; a 24× 50 mm one serves as the bottom and a 20×20 mm as the top. The microparticles are suspended in a solution of deionized water and sodium dodecyl sulfate (SDS) to prevent aggregation. We implemented Kohler illumination to ensure a uniformly illuminated bright field of view. The image is formed from light transmitted through an x100 objective lens (MRD01991, Nikon), achieving a pixel-to-spatial resolution of 51.0 nm/pixel, measured with a micro-calibration test target (USAF 1951, Thorlabs). We use a 1280x124 CMOS sensor camera (DCC1645C-HQ, Thorlabs) to optically inspect the sample, identifying, counting, and measuring the radii of the microparticles.

An external heat source, specifically a hot air gun, is positioned 15 to 20 cm away from the sample holder, with the distance adjusted to achieve the target temperature. The hot air gun provides a gentle airflow at a 30° angle of incidence to minimize vibration. Although the hot air temperature ranges from 100°C to 400°C, the actual temperature of the sample is significantly lower due to the distance and air convection. The temperature in the sample holder is digitally monitored using a thermocouple (TM-902C, Lutron) attached to the bottom, away from the direct airflow of the heat gun. Thermal paste guarantees proper thermal contact between the thermocouple and the glass holder. We varied the temperature from 18°C to 90°C, allowing us to control the environmental conditions affecting the Brownian motion of the microparticles. Besides, all electric systems are connected to uninterruptible power supply (UPS) sources to prevent electronic noise and to assure voltage stability.

3.1.1 Piezoelectric control signal

As mentioned earlier, the steering mirror is driven by a piezoelectric actuator, the current that drives this actuator is generated by a single-channel arbitrary function generator (AFG, AFG 3021B Tektronix) and then transmitted through a piezo-controller. An amplifier inside the piezo-controller, along with a malfunction of the AFG, causes a significant voltage amplification between the set value at the AFG and the actual output at the piezoelectric actuator. Table 3.1.1 shows

the voltage relationships between the set values at the AFG, the actual output measured at the AFG, and the voltage measured at the piezoelectric actuator. The total voltage amplification is approximately 31-fold.

V_{pp} Set at AFG	V_{pp} Measured at AFG	V_{pp} Measured at Piezoelectric	Multipliying factor
mV	mV	mV	-
100	232	3140	31.4
200	432	6320	31.6
300	640	9440	31.5
400	840	12500	31.3
500	1030	15800	31.6
1000	2120	31000	31.0
2000	4200	62000	31.0
3000	6240	-	-
4000	8320	-	-
5000	10400	-	-

Table 3.1.1: Voltage peak to peak (V_{pp}) used for piezoelectric control. Here are shown the values set at the AFG, the real output of the AFG and the measured V_{pp} at the piezoelectric actuator (PZA), the amplification of voltage between the AFG and the PZA is due to the Piezo-Controller. The multiplier factor is calculated as the ratio between the measured V_{pp} at the piezoelectric actuator and the one set at the AFG.

For values above 2000 mV (corresponding to about 62 V at the piezoelectric), we observed potential risks to the digital oscilloscope and the piezoelectric actuator and therefore did not measure these directly, as indicated by the dashes in Table 3.1.1.

The driven signal chosen for the system was a sinusoidal wave with a voltage peak-to-peak of 5 V, corresponding to a 155 V signal at the piezoelectric actuator. This signal was selected to ensure a displacement of the image of the sample on the EBC sensor large enough to generate abundant events. An offset of 2.5 V was added to the signal to avoid negative values, and the frequency was set to 1 kHz as the piezoelectric response was smooth in this range and it generate an abundant event rate. Nonetheless, some recordings were made with different frequencies to test the response of the system, and the data from one of them is shown in Figure 4.1.1 and 4.2.1, the frequency used was 700 Hz.

Note that the frequency chosen for the modulation signal is going to appear in different stages of the analysis, as in the frequency spectrum of the particle

trajectory, see figure 3.1.2, or in an histogram of the number of events detected by the EBC in a certain time window, as seen in figure 3.1.3, details on why this happens are going to be explained in the corresponding sections.

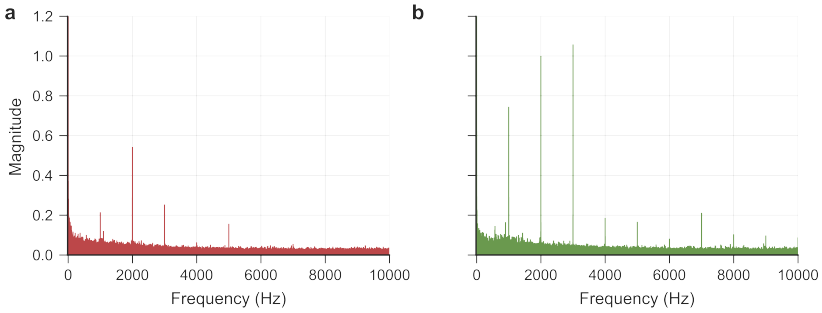

Figure 3.1.2: Spectrum for the measured particle trajectory. (a) x component and (b) y component, a peak at 1 kHz, which is the frequency of the modulation signal, and other peaks at multiples of the main peak can be observed. Before obtaining the spectrum is necessary to extract the position of the particle from the events detected by the EBC, but in this step some time window have zero events registered, and therefore no position is estimated. To avoid these "nan" values interpolation is applied to the data before calculating the spectrum.

3.1.2 Events acquisition protocol

We use an EBC (Gen3S1.1, Prophesee) with a sensor that has a resolution of 640 x 480 pixels, each pixel measuring 15 μm, and a dynamic range of 120 dB. Events were recorded using Metavision Studio version 3.1.2, the software provided by the manufacturer, which offers a graphical user interface (GUI) enabling control over critical sensor parameters required for acquisition. The acquisition process utilizes the full sensor size. While numerous micro-particles were present in the EBC field of view, we focused exclusively on freely moving single micro-particles within a specified ROI in the images. The ROI was established during the centroid computation process to validate our strategy. Once a particle is selected, the ROI and illumination conditions are configured and kept constant throughout the recording. Subsequently, the EBC GUI parameters are optimized to improve event detection. Despite these efforts, the number of detected events remains consistently insufficient, regardless of parameter adjustments. This limitation compels us to artificially boost the stream of events by controllably steering the image of the sample onto the EBC sensor.

The EBC is positioned at the image plane approximately 70 cm away, a distance

carefully selected to facilitate gentle adjustments of a steering mirror (BB1-E02, Thorlabs) in the image-forming path. This mirror is mounted on a kinematic gimbal mirror mount (KX1, Thorlabs) for precise steering control. A tilt angle is driven by a piezoelectric actuator connected to a 3-axis Piezo-Controller (MDT693A, Thorlabs) and controlled by a single-channel arbitrary function generator (3021B, Tektronix). The steering mirror increases the recorded stream of events by modulating the light from the sample at the image plane. As a result, a strong signal compensates for the insufficient number of events needed to estimate the position of the center of the microparticle every 50 μs.

3.1.3 Increase in the number of events

The effect of the optical modulation in the event rate is clearly visible while using the setup. Nonetheless, a more detailed analysis is required to understand the behavior of the system. Figure 4.1.1 shows the number of events detected by the EBC in a time window of 16 μs. From here, is clear that the increase in the number of events is not steady, instead it varies periodically with the same frequency as the modulation signal.

An explanation for this effect comes from the realization that the increase in the number of events is related to the displacement of the image of the sample on the sensor. And bu the modulation signal being sinusoidal, the displacement of the image and the number of events detected are also sinusoidal.

We propose the following mathematical description for the number of events detected by the EBC due to the modulation:

$$M(t) = -\left|A\cos(2\pi Bt + C)\right| + D\,, \tag{3.1.1}$$

this comes from the expected behavior for the speed at which the particle moves on the sensor. And in figure 3.1.3 we can see the result of fitting this function to the data. This function is not simply proportional to the speed of the particle induced by the modulation, and the hypothesis is that the exact shape of the function can be affected by the fact that the event are triggered by changes in the logarithm of the intensity of the pixel, and not by the intensity itself.

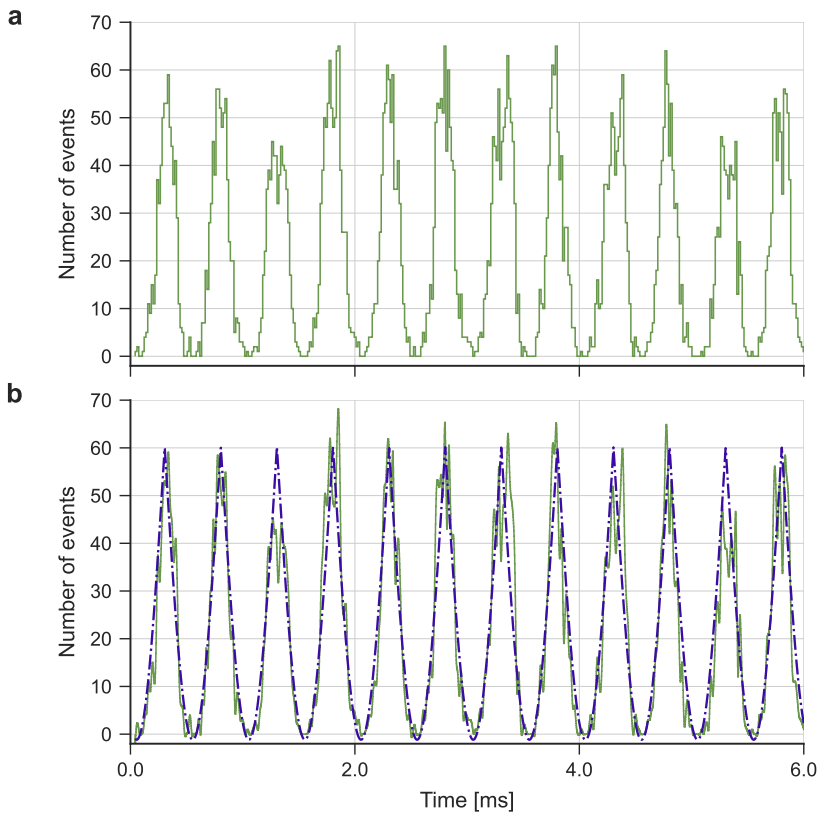

Figure 3.1.3: Events detected by the EBC in a time window of 16 μs. We can observe that the number of events detected shows a periodic behavior, this is related to the modulation signal used, and from a correct curvefit is possible to extract the frequency and phase of the modulation signal.

3.1.4 Displacement due to the modulation

Depending on the approach used to separate the brownian motion from the modulation signal, it could be useful to fully know the parameters of the modulation signal. By being sinusoidal, the parameters of interest are three: the frequency, the amplitude, and the phase.

Starting with the frequency characterization, we analyze the frequency spectrum of the measured particle trajectory. Figure 3.1.2 shows the power spectral density of a typical particle trajectory. A dominant peak is clearly visible at 1 kHz, corresponding to the fundamental frequency of our modulation signal. Additional peaks are observed at integer multiples (2 kHz, 3 kHz, etc.), representing higher harmonics that arise, probably, from the response of the optical system to the piezoelectric actuation.

The amplitude of the modulation signal is directly related to the displacement of the image of the sample on the sensor, and it can be easily obtained from the curve for MSD as a function of τ. As we will see in the subsection 3.5.2, the modulation signal introduces a periodic component in the MSD curve and the amplitude of the resulting curve is equal to the square of the amplitude of the modulation signal.

Finally, the phase of the modulation signal is obtained from the curve fitting of the number of events detected by the EBC using equation (3.1.1). This resulting phase might differ from the one set at the arbitrary function generator by $\pi/2$ due to the nature of the cosine function.

3.2 Pixel-to-spatial resolution of the EBC

The pixel-to-spatial resolution (51.0 nm/pixel) for the EBC was measured using a micro-calibration test target, specifically a Negative USAF 1951. Being a negative test target means the reference lines are transparent while the background is opaque. The target is illuminated with a light source, and the image is captured by the EBC similarly to the microparticles visualization. Since the target is a still image, the events detected by the EBC result from noise in the sensor in areas of high illumination. Events within the region of the calibration bars accumulate over time, so with a sufficiently long recording, the test target becomes visible in the event data. An example of this can be seen in panel a from figure 3.2.1.

The list of events is converted into a density plot counting the number of events detected by each pixel, resulting in an image of the calibration bars similar to that produced by a classical camera. From this, the width of the bar in pixels can be obtained, the inclination relative to the sensor array can be compensated, and the pixel-to-spatial resolution ratio can be calculated. This steps can be visualized at panel b and c from figure 3.2.1.

3.3 Measuring the radius of the particles

Commercially available microparticles exist in a wide variety of sizes and compositions, typically they come in a well labeled container with information about sizes, densities, and other characteristics. However, it is important to verify

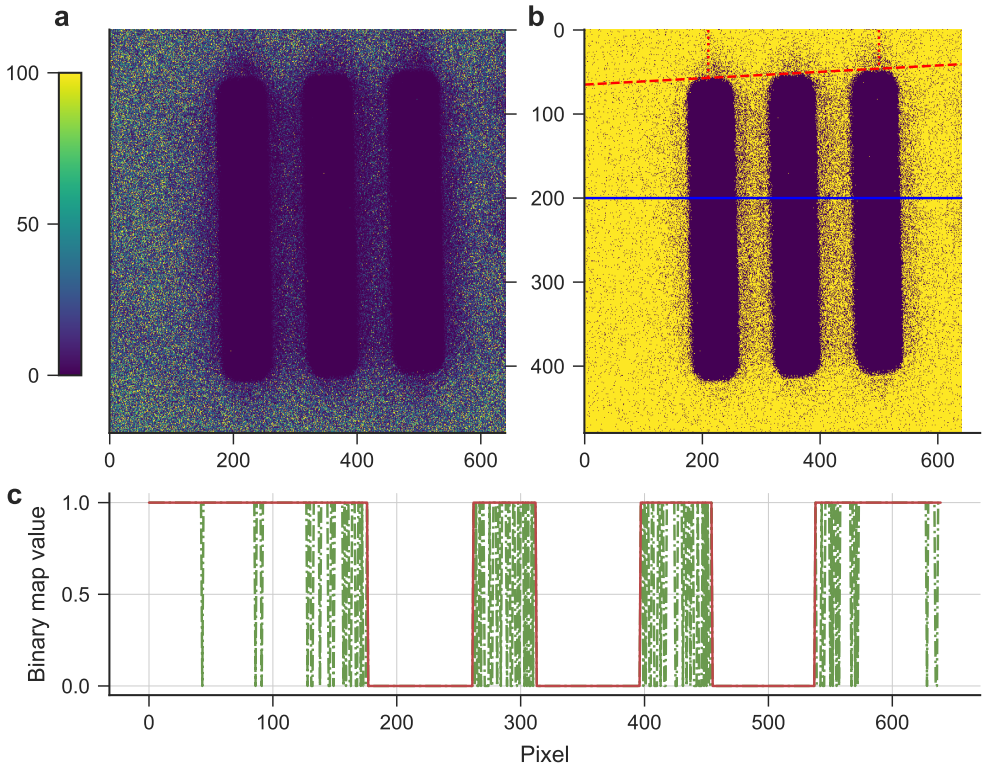

Figure 3.2.1: Steps to measure the pixel-to-spatial resolution of the EBC. (a) Colormap showing how many events were registered by each pixels in the recording of the negative test target with the EBC, with a maximum value of 100. The lines observed corresponds to group 7, element 2. (b) All pixels that detected at least one event are set to the same value. The blue solid line represents the line used to estimate the width of each line, and the red dashed lines gives the idea of how inclination is measured to then be considered in the resolution. (c) The green dashed line shows how the line obtained from panel b looks like, and the red solid line is the result after filtering isolated pixels with no events.

some of the properties experimentally, as the particles may have been damaged or contaminated during handling. To measure the radius of the microparticles, we use a CMOS sensor camera (DCC1645C-HQ, Thorlabs) to optically inspect the sample. The camera is connected to a computer running the software provided by the manufacturer, ThorCam, which allows us to visualize the sample and save images.

Two collections of images were taken, each one at different concentration of particles, they were obtained from already prepared samples that were preserved at low temperature in a refrigerator. Several images were taken for a single scene at different focal lengths, and the best one was selected for further analysis. The images were processed to identify the microparticles and measure their radii, to

do so, the following steps were taken:

1. Convert the image to grayscale.
2. Apply a Gaussian blur to reduce noise.
3. Apply a HoughCircles algorithm to detect circles in the image, choosing the correct parameters said circles corresponds with the particles.
4. Identify pairs of particles that are really close to each other, and measure the distance between them. This distance will be considered as the diameter of the particles.

   Note: To convert from pixels to longitude units we need a conversion factor previously obtained by calibrating the system using a test target, in particular, we made use of a Negative USAF 1951.

The idea behind the last step is to avoid the need to identify precisely the border of a particle, which can be difficult due to the low contrast between the particle and the background and the apparent variation of it while changes the distance between the sample and the objective lens. Instead, the method with pairs of particles is more robust and less sensitive to the image quality. An example of the process is shown in Figure 3.3.1.

3.4 Particle identification and tracking

Figure 3.4.1 illustrates the process of converting events into positions. The EBC records events, which are stored as a list where each event is represented by four values: the x and y coordinates, the event polarity, and the timestamp. For this particular EBC, the x and y coordinates range from 0 to 639 and 0 to 479, respectively, representing the pixel positions where the event was detected. The polarity is a binary value that indicates whether the event signifies an increase or decrease in pixel intensity. The timestamp denotes the time at which the event was detected and is saved as an integer value representing the time in microseconds since the recording began.

After importing the list of events as a dataframe, the data is processed to determine the position of the particle. The first step is to group the events into segments based on a predefined acquisition time, t_{acq}. All the events contained in a segment

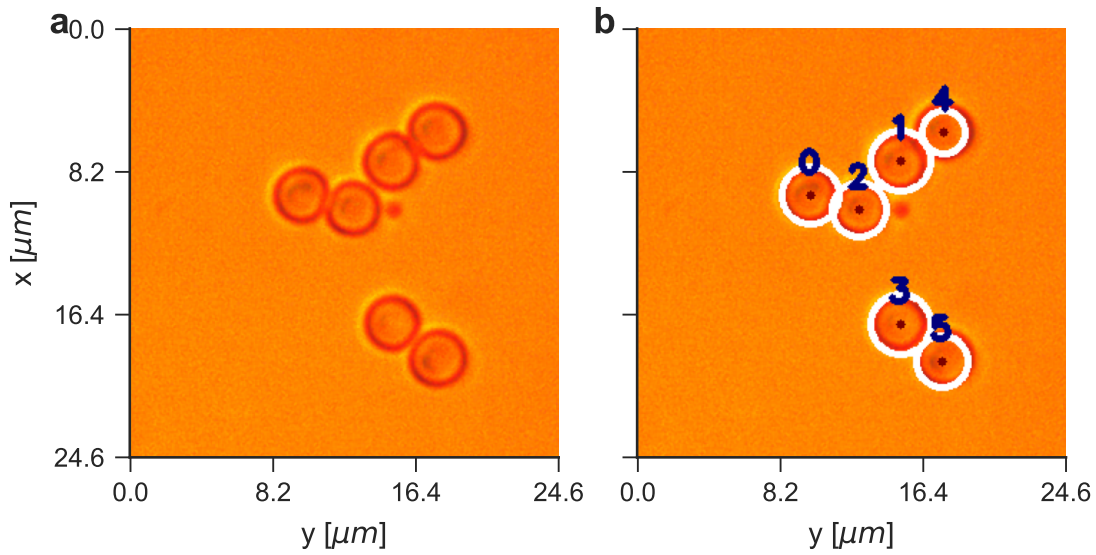

Figure 3.3.1: Representation of the process to measure the radius of the microparticles. (a) Three pairs of particles close together are shown, this is a cut from the whole image. (b) Here the particles are identified and labeled, by choosing the label for a pair, we can obtain the distance between their centers in pixels to then convert to longitude using the calibration of the system. Note that the calibration is different from the one used for the EBC.

are used to estimate a single point in the particle's trajectory. To obtain this point, the events from the segment are separated by polarity, and for each polarity, X_p and Y_p positions are calculated as the median of the x and y values, the median is used instead of the mean to gain robustness in situations where high levels of noise are present. The final position of the particle is then determined as the mean of the X_p and Y_p positions.

Given that the standard error of the median is inversely proportional to the square root of the number of events, the number of events in each segment is crucial for precise position estimation. This implies that a higher event rate will result in a more precise position estimation for the same acquisition time t_{acq}.

3.5 Characterizing diffusion from displacement

To characterize the diffusion properties of Brownian particles and their dependence with temperature, we implemented a temperature control system consisting of a hot air gun and thermocouple as described in Section 3.1. This system allowed us to regulate the sample temperature across a range from 19°C to 75°C, with the

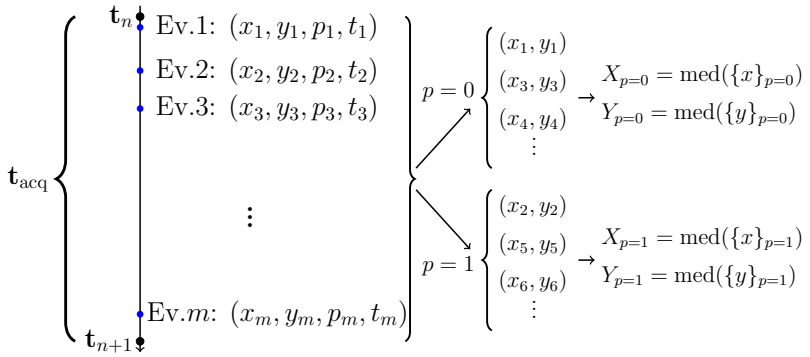

Figure 3.4.1: Events processing algorithm diagram. A visualization of how events are processed to obtain the position of the center of the particle.

upper limit dictated by the thermal tolerance of the nail polish used to seal the sample chambers. By observing particle motion at various temperatures, we could validate our tracking methodology against theoretical predictions while exploring the temperature dependence of the diffusion coefficient.

3.5.1 Mean square displacement calculation

The mean square displacement (MSD) serves as the primary analytical tool for extracting diffusion coefficients from particle trajectories. For our experimental data, we calculate the MSD as a function of the time interval τ from the trajectory of each tracked particle, represented by a series of position vectors $\vec{r}_i = (x_i, y_i)$ for $i = 1, \ldots, N$, recorded at regular time intervals Δt.

For any two positions $\vec{r}_i$ and $\vec{r}_j$, the displacement is defined as $\Delta\vec{r}_{ij} = \vec{r}_j - \vec{r}_i$, corresponding to a time interval $\tau = (j - i)\Delta t$. Consequently, the MSD for a given time interval $\tau = n\Delta t$ is expressed as

$$\text{MSD}_{\text{2D}}(\tau) = \frac{1}{N-n} \sum_{i=1}^{N-n} \left|\vec{r}_{i+n} - \vec{r}_i\right|^2 , \tag{3.5.1}$$

and, in a similar way, the MSD in one dimension is given by

$$\text{MSD}_{\text{1D}}(\tau) = \frac{1}{N-n} \sum_{i=1}^{N-n} \left(r_{i+n} - r_i\right)^2 . \tag{3.5.2}$$

In our experimental setup, each position vector $\vec{r}_i = (x_i, y_i)$ represents the centroid of the microsphere, calculated as described in Section 3.5 from the coordinates

of events detected by the event-based camera within a defined temporal window, most typically of 50 μs.

3.5.2 Considerations for experimental reproducibility

Two key considerations must be addressed to ensure reproducible diffusion measurements in our experimental setup.

First, the presence of sodium dodecyl sulfate (SDS), a surfactant, in our sample preparation raises questions about its impact on the dynamic viscosity of the fluid, which directly affects the diffusion coefficient. While SDS is well-known for lowering the surface tension of water, its effect on dynamic viscosity is not thoroughly documented in the existing literature. From our sample preparations, we observe that the concentration of SDS is less than 0.1 [g/100ml], and as noted in the work of Kushner et al. [48], the effect of SDS on the viscosity of water reflects as a variation of 0.69% for a concentration of 0.1 [g/100ml] at 23°C. Therefore, in this work, we assume that the effect of SDS on the viscosity of water is negligible.

Second, and more significantly, our optical modulation method introduces a challenge for MSD analysis. While the diffusion coefficient can theoretically be extracted through a linear fit to the MSD curve, our measured particle positions combine natural Brownian motion with the superimposed sinusoidal displacement caused by the steering mirror. This combined motion creates a periodic component in the MSD curve that obscures its expected linear behavior, as shown in Figure 3.5.1.

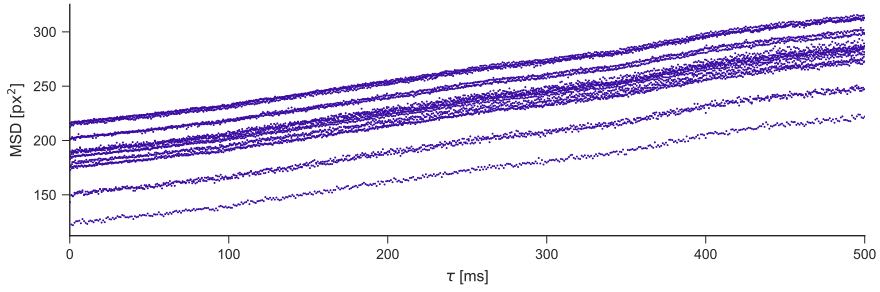

Figure 3.5.1: MSD vs τ curve from the superposition of particle motion and modulation. From theory, we expect a linear behavior for the MSD vs τ curve when considering only Brownian motion, but the modulation introduces a periodic component superimposed on the linear trend. This makes the curve appear as several parallel lines with slight vertical offsets.

To better understand this effect, we performed simulations with computationally generated Brownian trajectories, both with and without added sinusoidal modulation. Figure 3.5.2 illustrates how the addition of a sinusoidal component affects both the trajectory itself and the resulting MSD curve.

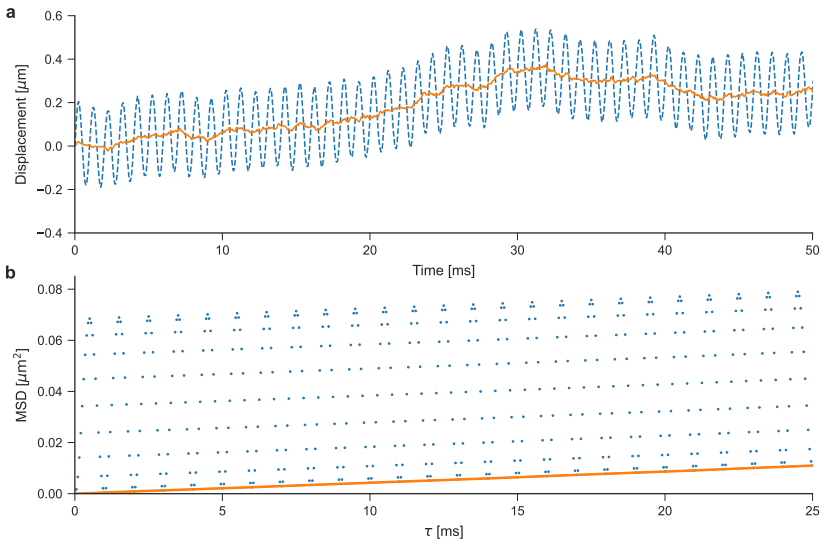

Figure 3.5.2: Effect of sinusoidal modulation on the MSD curve. Using a computationally generated Brownian trajectory, we can clearly observe the impact of sinusoidal modulation on the MSD behavior. (a) One component of the Brownian trajectory with and without sinusoidal modulation. (b) The MSD vs τ curve for the Brownian trajectory with and without sinusoidal modulation, showing how the sinusoidal component introduces oscillations while preserving the underlying slope.

Importantly, our simulations confirm that despite the oscillatory behavior introduced by the modulation, the slope of the MSD curve remains preserved. This is evident in Figure 3.5.3, where the MSD curve from modulated data can be separated into multiple parallel lines, all sharing the same slope but with different vertical offsets.

Additionally, the statistical reliability of MSD calculations also depends on the amount of displacement measures available for averaging. Figure 3.5.4 shows that the variance in MSD estimates increases for larger τ values if the length of the trajectory remains constant. This effect must be considered to determine how long the recordings should be to ensure a statistically reliable calculation of the diffusion coefficient.

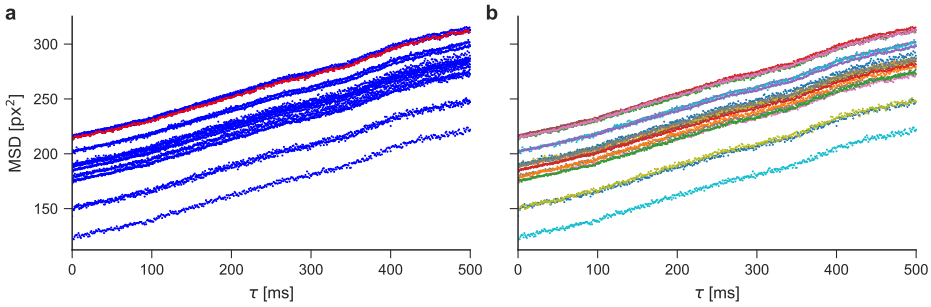

Figure 3.5.3: Separation of the MSD curve with modulation into component lines. The MSD data from modulated trajectories can be decomposed into multiple parallel lines (shown in different colors), each corresponding to a specific phase relationship with the modulation signal. All lines share the same slope (related to the diffusion coefficient) but have different vertical offsets caused by the periodic modulation.

3.5.3 Methods for extracting diffusion coefficients from modulated trajectories

Based on our understanding of how optical modulation affects MSD curves, we developed and evaluated three distinct methods to accurately extract diffusion coefficients from our experimental data:

1. **Mean Curve Method:** This approach involves separating the MSD curve into subsets based on the modulation period, then averaging these subsets to obtain a mean MSD curve that minimizes the periodic component.

2. **Lowest Curve Method:** This method identifies and isolates the lowest of the parallel MSD curves, which represents the trajectory points with minimal contribution from the modulation signal.

3. **Frequency Filtering Method:** This technique applies band-stop filters to remove the modulation frequency components from the position data before calculating the MSD curve. As a result of this, the MSD curve displays a linear behavior.

For all the methods, the trajectory data was segmented into 3-second clips before calculating the MSD curve. The relevant factor in determining the length of the clips is the number of measures contained within each clip, as a statistically reliable calculation of the MSD depends on the number of points used [49]. See figure 3.5.4.

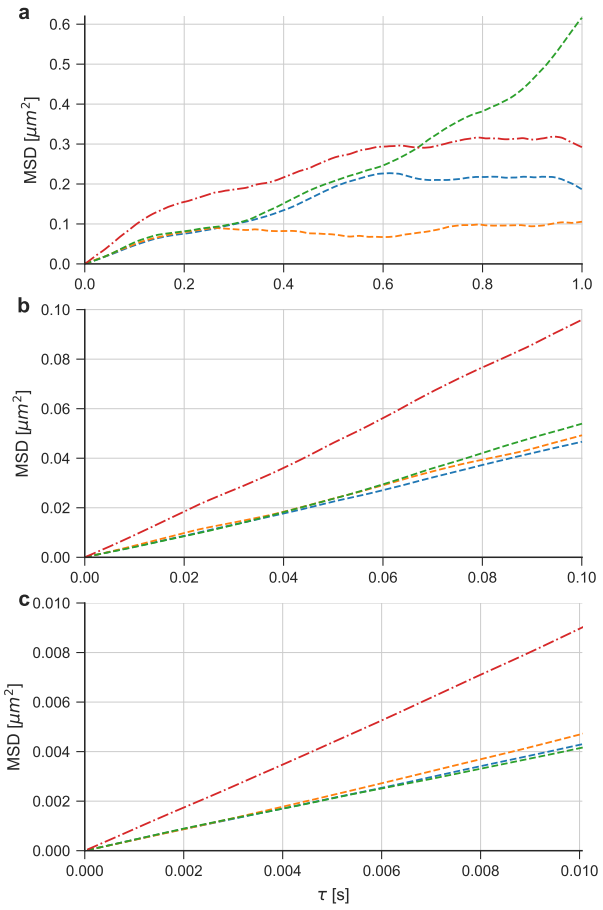

Figure 3.5.4: Statistical stability of the MSD curve at different time intervals. The uncertainty in MSD estimates increases with larger τ values due to the decreasing number of independent displacement samples available for averaging. This effect must be considered when determining the appropriate range of τ values for diffusion coefficient extraction.

To compare the performance of these methods will be necessary to look at figure composed by different plots showing the different results. But the the elements in each one are rather similar, and would be easier to introduce the general idea of how the results will be presented before showing the plots. An standard figure with the results of the methods is shown in figure 3.5.5, here we observe a plot of Diffusion coefficient versus temperature, in the background we observe a colored region representing the expected value for the diffusion coefficient for particles with a radii between 1.4 and 1.6 μm, the measured values are expected to be in this region, orange dots represent the diffusion coefficient obtained for each clip, and then by separating the clips into temperature ranges and taking the average over all the values, we obtain the purple dots, with an error bar representing the

reduced error of the average. For all the following figures, clips are grouped in temperature ranges of 5°C.

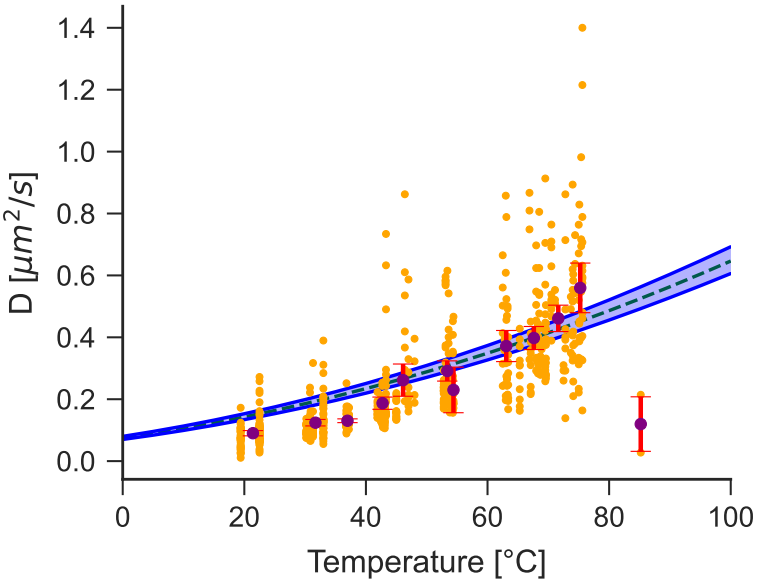

Figure 3.5.5: Example on how the resulting diffusion coefficient will be displayed. Here we can observe a colored region representing the expected value for the diffusion coefficient for particles between 1.4 and 1.6 μm in diameter, orange dots represent the diffusion coefficient obtained for each clip, and then by separating the clips into temperature ranges and taking the average over all the values, we obtain the purple dots, with an error bar representing the reduced error of the average.

In the following subsections, we detail each method and present their results, followed by a comparative analysis of their performance.

3.5.4 Method 1: Mean curve from MSD data

The first approach for extracting the diffusion coefficient from modulated trajectories tries to obtain a single curve by averaging all the ones that can be identified in the MSD curve. This method follows a systematic process:

1. **Data segmentation:** We begin by dividing the recorded trajectory into fixed-length segments, we choose 3 seconds long clips. This duration provides sufficient data points to ensure statistical reliability while maintaining manageable computational requirements, and having a high amount of clips allows us to increase the amount of independent samples for the diffusion coefficient estimation.

2. **MSD calculation:** For each segment, we calculate the mean square

displacement (MSD) as a function of time lag τ, focusing on a region where the MSD is statistically stable (typically for τ values up to approximately 10% of the total segment duration).

3. **Periodicity identification:** We identify the frequency of the periodic component in the MSD curve, which matches the modulation frequency of 1 kHz. With our acquisition time step of 50 μs, each complete cycle of the modulation corresponds to 20 consecutive data points in the MSD curve. You should be careful if the period cannot be covered by an exact number of points, in this case, the method will not work as expected.

4. **Subset creation and averaging:** Based on this periodicity, we decompose the MSD curve into consecutive subsets of 20 points each, and each subset will obtain a new time stamp, that can be the mean of all the originals, the lowest one, or other option, the important thing is to do it consistently. After this, we average the 20 elements of each subset to obtain a new MSD curve that minimizes the periodic component.

5. **Diffusion coefficient extraction:** Finally, we perform a linear fit to this mean MSD curve according to the relation $\mathrm{MSD}_{1\mathrm{D}}(\tau) = 2D\tau + \epsilon$, where D is the diffusion coefficient and ϵ represents the localization error offset.

The effectiveness of this method relies on the assumption that the modulation-induced component in the MSD curve is truly periodic with a well-defined frequency. When this condition is met, the averaging process effectively cancels out the modulation effects while preserving the linear trend that characterizes pure Brownian motion. Figure 3.5.6 shows the diffusion coefficients obtained using this method for 3-second clips across different temperature conditions, we can observe that for the three amount of points considered the results are close to the expected value, and as the amount of points increases the dispersion of the points decreases, but they tend to concentrate below the expected value. This might indicate that considering 80 points might be excessive, and allows to capture the error induced by insufficient data points to calculate the MSD.

Note that, due to converting 20 points from the MSD into just one, the time step between values of τ for the MSD curve is increased. This could be a factor to consider when estimating the ideal amount of points required for a reliable estimation of the MSD slope.

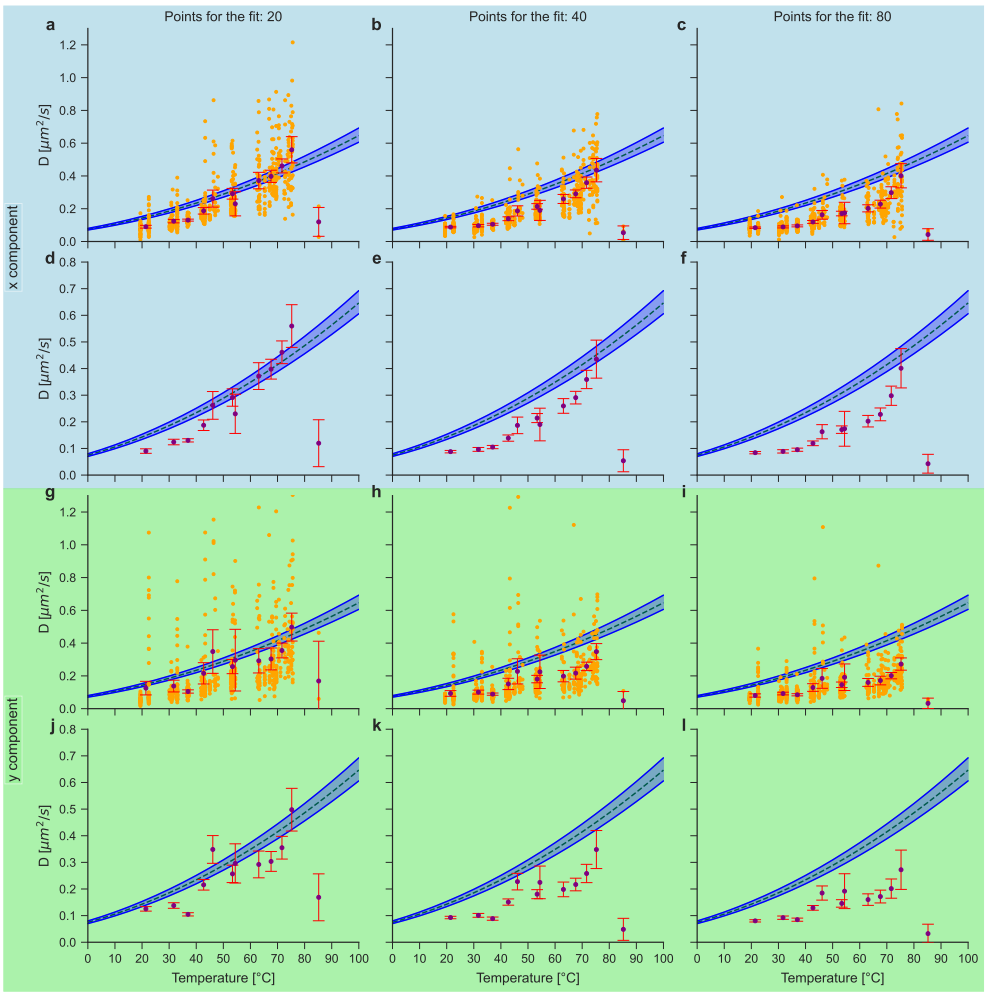

Figure 3.5.6: Measured diffusion coefficient using method 1, 3 seconds clips and different amounts of points. For each column a different amount of points from the MSD curve were used to fit the linear model, from left to right were used 20, 40 and 80, this is equivalent to 20, 40 and 80 ms. The upper rows use x dimension displacements, and the lower rows use y dimension ones.

3.5.5 Method 2: Lowest curve from MSD data

The second approach focuses on isolating one of the many curves identified in the MSD curve, we choose to focus in the one with the lowest values, as this should be the one with the least influence from the modulation signal. This method follows a similar process to the first one, but with a key difference in how we handle the MSD data after identifying the periodic pattern:

1. **Data segmentation.**

2. **MSD calculation.**

3. **Periodicity identification.**

4. **Lowest curve identification:** After identifying the periodicity, we decompose the MSD curve into subsets spamming over a whole period, 20 points in our case. Then we take a certain amount of these subsets, for example 15, and for each one, we identify the index that corresponds to the point with the minimum MSD value. We then determine which index appears most frequently across all examined subsets as the one consistently producing the lowest points. Using this most common index, we extract a single subset $C_m = \{d[m], d[m+20], d[m+2\cdot 20], \dots\}$ from the entire MSD curve, where m is the identified index and $d[i]$ represents the i-th point of the original MSD curve.

5. **Diffusion coefficient extraction:** We perform a linear fit to this lowest MSD curve according to the relation $\mathrm{MSD}_{1\mathrm{D}}(\tau) = 2D\tau + \epsilon$.

The idea of testing this method comes from what we can observe from figure 3.5.2, where the lowest points of the MSD from the motion with modulation coincides with the original brownian motion MSD. As was the case for method 1, here we also convert 20 points from the MSD into one, resulting in a larger time step between values of τ.

Figure 3.5.7 shows the diffusion coefficients obtained using this method for 3-second clips across different temperature conditions, demonstrating results comparable to the mean curve method but with slight differences in uncertainty characteristics. Here, the same time windows were used as in the previous method, and the results are as expected, showing larger dispersion when considering less points, and concentrating below the expected values when considering more points. The results from considering 20 points are far from the theoretical model, this might indicate that 20 points are not enough to capture the behavior of the MSD curve.

3.5.6 Method 3: Apply frequency filters before calculating the MSD

While the previous two methods focused on processing the resulting MSD curve to filter the linear behavior, our third approach focus on filtering the trajectory data before calculating the MSD.

For this, we selected fourth-order Butterworth band-stop filters due to their

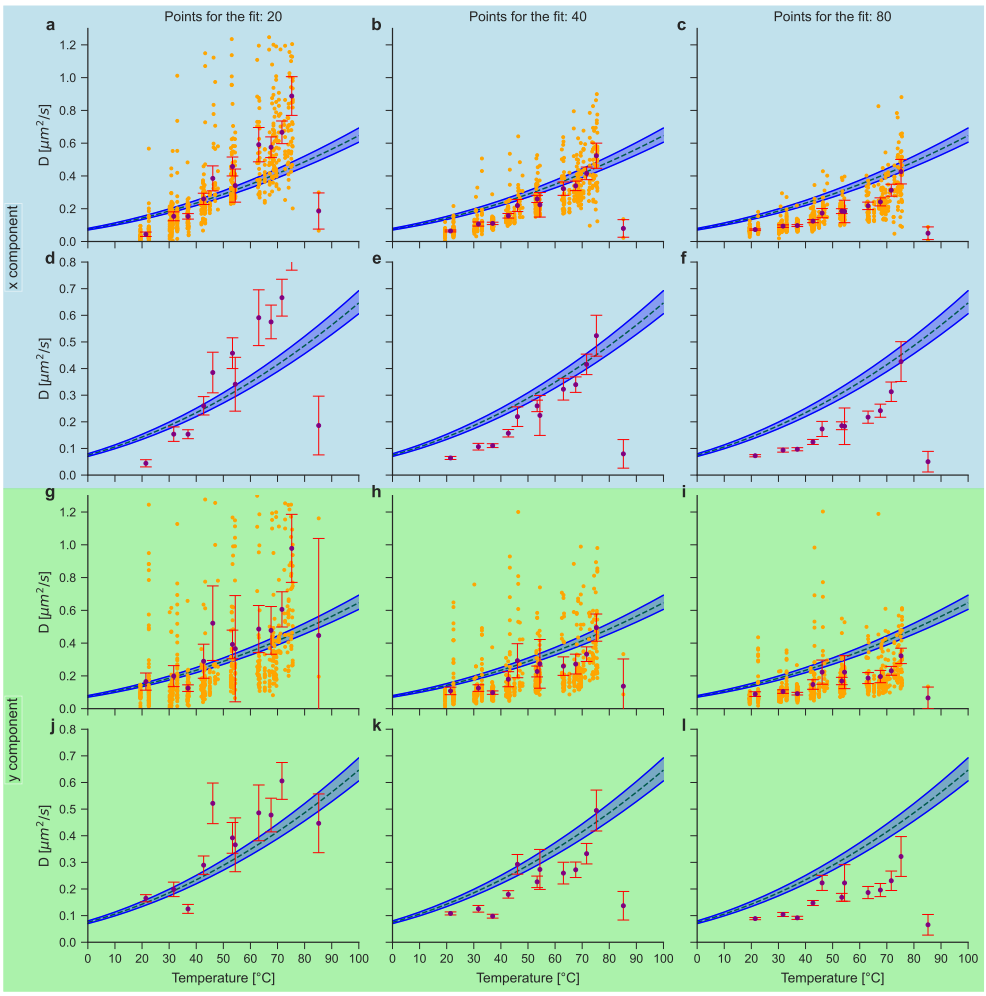

Figure 3.5.7: Measured diffusion coefficient using method 2, 3 seconds clips and different amounts of points. For each column a different amount of points from the MSD curve were used to fit the linear model, from left to right were used 20, 40 and 80, this is equivalent to 20, 40 and 80 ms. The upper rows use x dimension displacements, and the lower rows use y dimension ones.

maximally flat passband response, which minimizes distortion of the underlying Brownian motion signal [30]. The filters were centered at 1, 2, 3, 4, 5, 6, and 7 kHz, each with a 6 Hz bandwidth, the idea is to eliminate the frequency introduced by the modulation and their harmonics. The resulting filter was applied systematically using cascaded second-order sections to preserve causality [50], about this method is important to mention that the first points of the trajectory will be less reliable as the information available for the filtering is limited, for example when modifying a point at position n in the trajectory only information from the previous $n-1$ points is used.

The frequency filtering method follows these steps:

1. **Raw data preparation:** Unlike the previous methods, we begin with the complete trajectory dataset for each recording. This is important as it helps to reduce the impact on the first points due to the use of cascaded second-order sections while applying the filter.

2. **Linear interpolation:** We apply linear interpolation to address any gaps in the data due to insufficient events in certain time windows, this is necessary because the cascaded second-order sections method requires equally spaced information. Linear interpolation was selected over more complex methods because it performs well with stochastic processes without introducing artificial frequency peaks in the spectrum.

3. **Frequency filtering:** Then we apply the previously described frequency filtering, the combined frequency response of the filters is shown in figure 3.5.8. And their effect on the spectrum of a single recording is shown in figure 3.5.9.

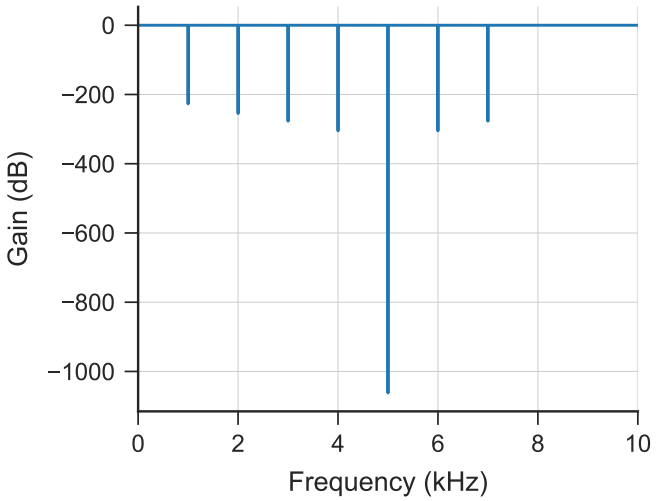

Figure 3.5.8: Frequency response of the filter used to remove the sinusoidal modulation. This is the resulting frequency response from the seven band-stop filters applied to the trajectory data.

4. **Data segmentation:** After filtering, we divide the trajectory into 3-second clips. Importantly, any remaining points that are not enough to form a complete clip are discarded from the beginning of the recording rather than the end. This approach minimizes the effect of the less reliable initial filtered points.

5. **MSD calculation and linear fitting:** For each filtered clip, we calculate the

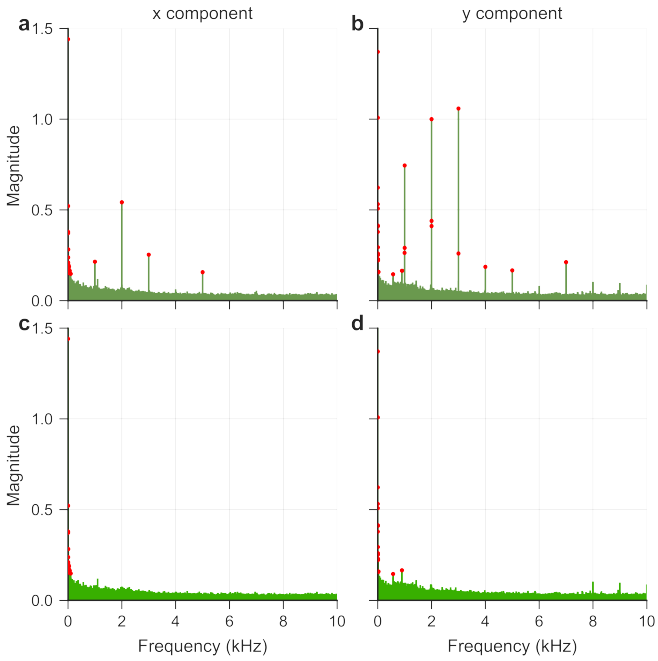

Figure 3.5.9: Spectrum of single clip before (upper panels) and after (lower panels) applying the frequency filter. Here we can observe how the frequency filter from figure 3.5.8 affects the spectrum of a single recording. Each column corresponds to the spectrum from a different dimension, x or y. And the red dots indicate the peaks identified using a prominence threshold of 0.14.

MSD curve and perform a linear fit to extract the diffusion coefficient.

A key advantage of this method is that it preserves the original temporal resolution of the MSD curve, unlike Methods 1 and 2. However, the method requires careful selection of filter parameters to avoid introducing artifacts or removing important components of the Brownian motion itself.

Figure 3.5.10 shows the diffusion coefficients obtained using this frequency filtering method across different temperature conditions, demonstrating consistent results that align well with theoretical predictions. For this case, smaller time windows were considered, consider that the smallest one used for methods 1 and 2 was 20 ms, and here that is the biggest. From this, we can observe that below 20 ms results are dominated by noise and the results are not near the expected values. But even for 20 ms, results are close to the expected values using this method.

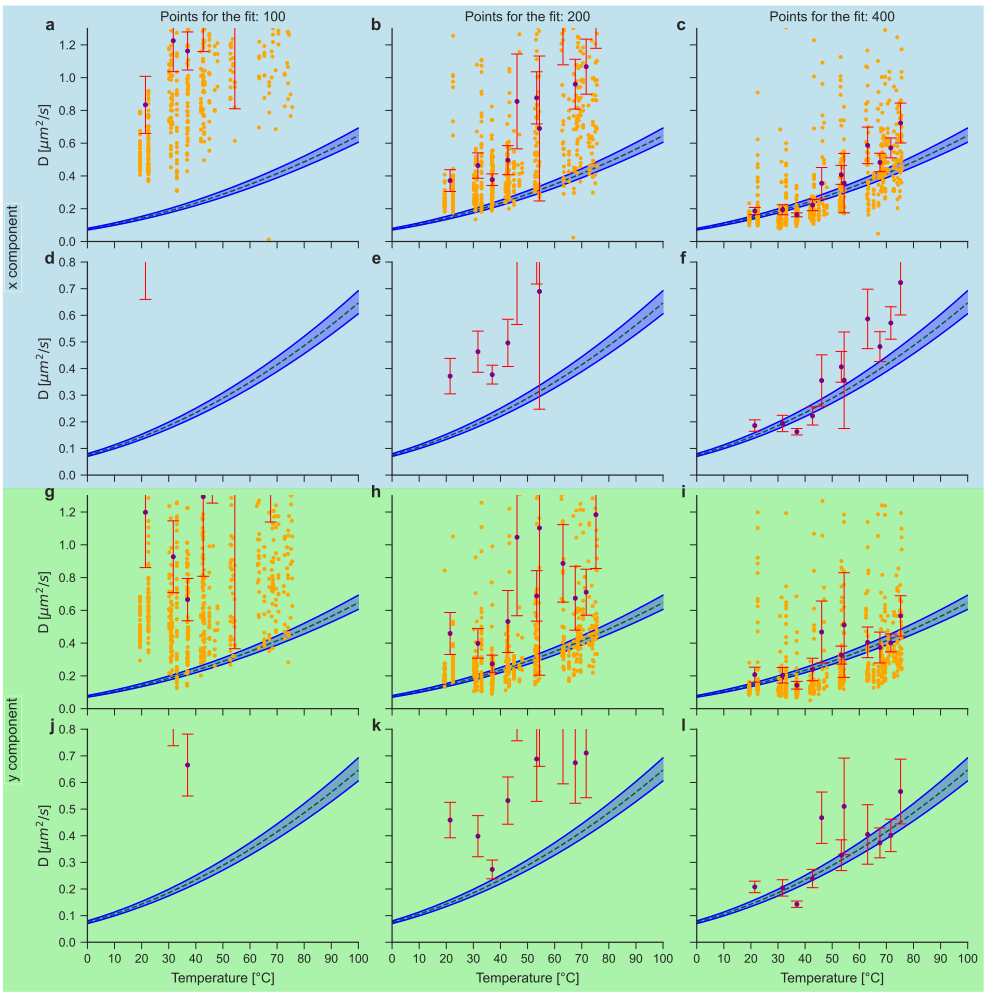

Figure 3.5.10: Measured diffusion coefficient using method 3, 3 seconds clips and different amounts of points. For each column a different amount of points from the MSD curve were used to fit the linear model, from left to right were used 100, 200 and 400, this is equivalent to 5, 10 and 20 ms. The upper rows use x dimension displacements, and the lower rows use y dimension ones.

3.5.7 Comparison of results

Finally, we combine in one figure 3.5.11 the results obtained from the three methods for the same set of recordings, using the same time window for the fit (40 ms) and the same size for the temperature segments (5°C). From this, we can observe that the results from the three methods are consistent with each other. But for this case in particular, the results from method 1 (mean curve) describe a curve below the expected one. And in method 3 (frequency filtering) the average over a region around 55°C has a unexpectedly big error bar. This might indicate that the method is not as robust as the other two.

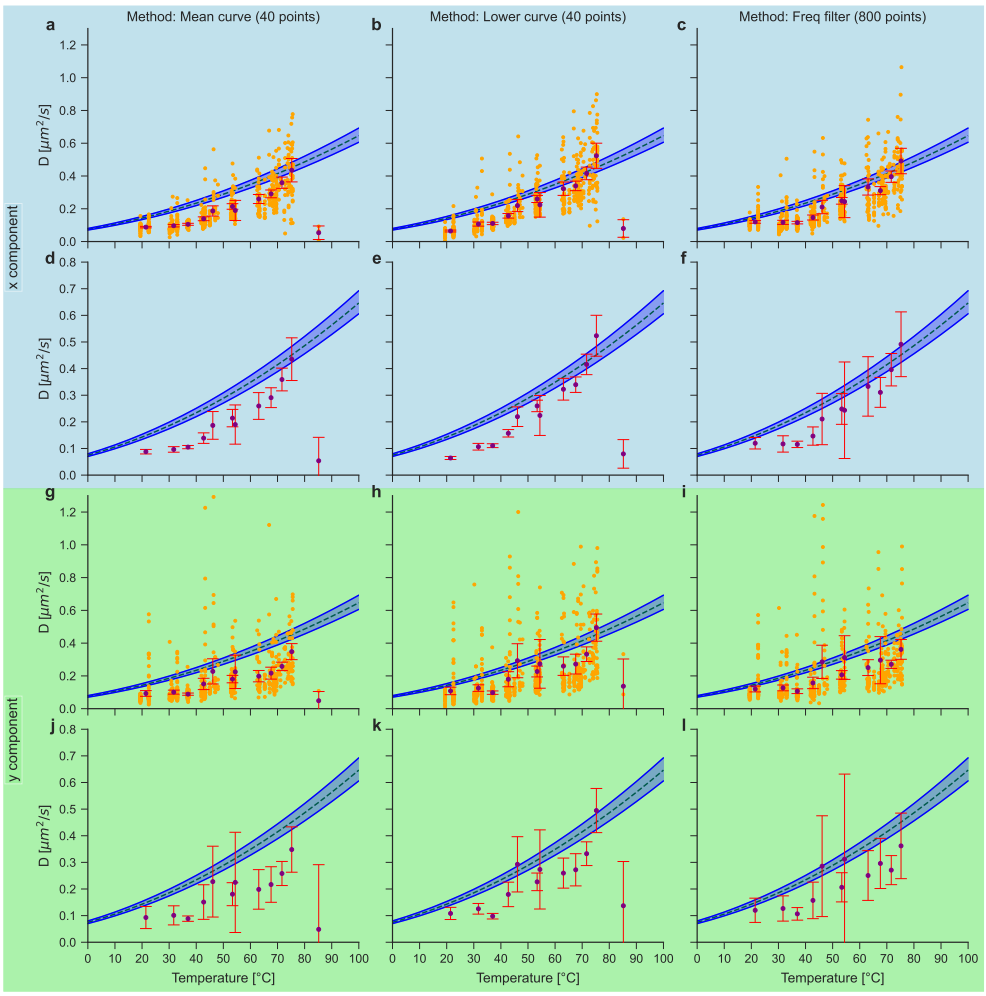

Figure 3.5.11: Comparison between methods to determine the diffusion coefficient. The upper rows use x dimension displacements, and the lower rows use y dimension ones. For each column a different method was used, the amount of points were choosen so the three cases use a section of 40 ms.

3.6 Permutation entropy and statistical complexity calculations

To calculate PE and SC values we made use of the python package *ordpy*, in particular the function **complexity_entropy** that takes as input the list of values to analyze, the embedding dimension, and time delay. An the output is a tuple with the PE and SC values, note that the resulting PE value is already normalized, so they are directly comparable between different embedding dimensions.

In our study, all the PE and SC values analyzed were obtained from the same

3 second clips used to obtain the diffusion coefficients with methods 1 and 2. Considering that all the recordings were processed using an acquisition time of 50 μs, the number of points in each clip was 60000.

About the parameters for the function:

- The embedding dimension (m) was set to 6. This value was chosen on the criteria of that $m! \ll N$ where N is the length of the series to obtain reliable PE values, while this usually translated as $m! < 10 \cdot N$ and an embedding dimension of 7 would satisfy it, we chose 6 to have a more conservative approach.
- The time delay was set to 1, this is the most common value used in the literature to study Fractional Brownian motion [42].

The resulting distribution of points in the complexity-entropy plane for two particular recordings is shown in figure 3.6.1, where we can observe that the points are distributed along a curve, similar to what is observe in the case of fBm. But the exact point of the curve that they group around is different for each recording and component.

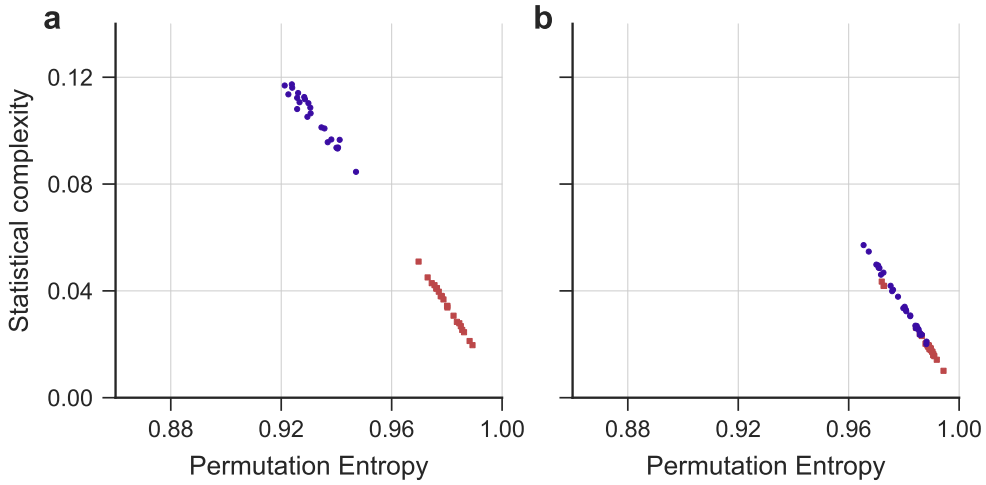

Figure 3.6.1: Complexity-entropy plane for all the clips obtained from a single recording. Here two files with similar characteristics were divided into clips and by displacement component, and the PE and SC values were calculated for each one. Red squares correspond to the x component and blue circles to the y component.

From the elements previously described and interesting question arise, how does the frequency filtering affect the PE and SC values? To answer this question we applied several butterworth band-stop filters centered each one at an integer

multiple of the modulation frequency, and then we calculated the PE and SC values for the resulting trajectories. The results are shown in figure 3.6.2, where we can observe that the PE and SC values are displaced along the curve for fBm in the complexity-entropy plane, this displacement drives the point to a region with lower SC and higher PE, which is consistent with the idea that the filtering is removing the periodic component of the signal.

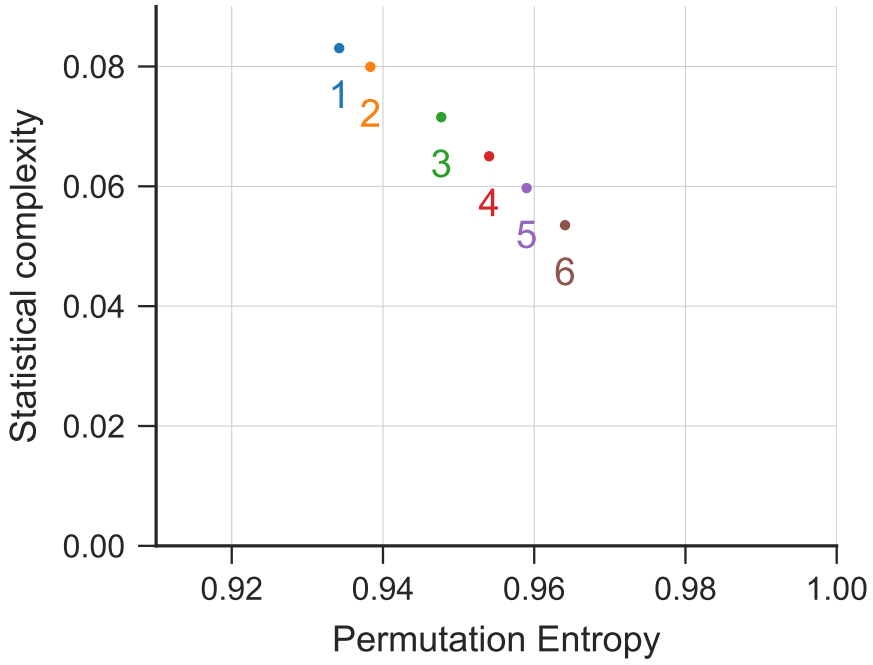

Figure 3.6.2: Displacement in complexity-entropy plane due to frequency filtering. We take a single recording and calculate the PE and SC values for the one of component of the displacement, then we apply a band-stop filter centered at 1 kHz and calculate the PE and SC values again, and repeat this process for filters centered at 2, 3, 4,and 5 kHz. As a result we can observe that the PE and SC values are displaced to the right along the curve for fBm in the complexity-entropy plane. 1: no filter, 2: + 1 kHz, 3: + 2 kHz, 4: + 3 kHz, 5: + 4 kHz, 6: + 5 kHz.

Chapter 4

Analysis of results

4.1 Effect of the optical modulation in the number of events detected

Figure 4.1.1a shows the number of events detected by the EBC within a 50 μs time window before and after activating the steering mirror. This data is recorded continuously to capture the effects of an abrupt turn-on.

The modulation significantly affects the number of events, increasing the average number of events per time window 0.4 before modulation to 161.8 after modulation begins. This is equivalent to going from 1 event every 125 μs to 1 event every 0.309 μs, or a 404-fold increase in the event rate. However, the event rate is not constant when the image is steered sinusoidally; instead, we observe a periodic increase and decrease in the number of events, fluctuating from 0 to around 300. This pattern corresponds with the increase in the speed at which the image of the particle moves through the sensor due to the steering mirror.

From this, we note that at different moments in the recording, we observe different streams of events and, consequently, different object resolutions. Three segments were selected and displayed for comparison in Fig. 4.1.1b. Events are included in a colormap, and positions estimated from the algorithm explained in 3.4 are overlaid for reference. Frame 1 shows a segment before the modulation is activated; in this case, only four events are registered, making the situation easily influenced by noise. Frame 2 is taken from near a minimum of events with the modulation

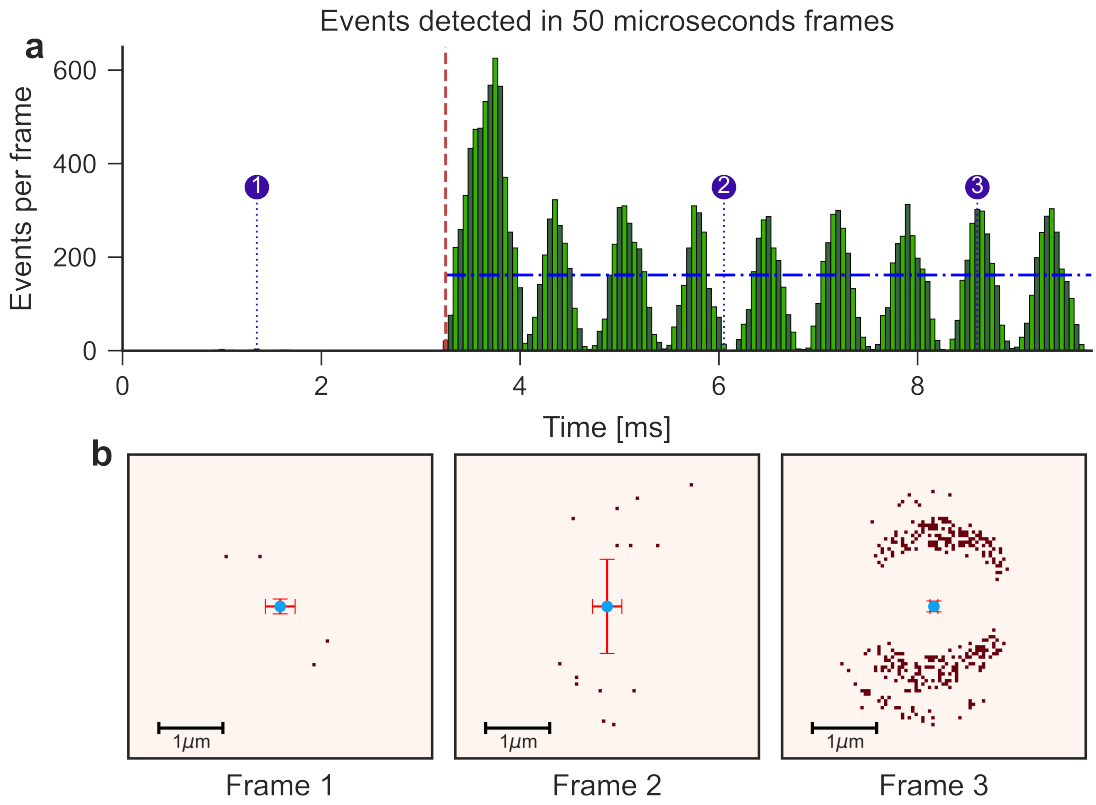

Figure 4.1.1: Effect of the optical modulation in the number of events detected. (a) Number of events detected in 50 μs windows, with the piezoelectric device activated around the 3 ms mark (red dashed line). The blue line represents the average number of events during the modulation. (b) Three sets of events are displayed, each corresponding to a 50 μs segment, with each dark square representing a pixel of the camera. Both event polarizations are included. The moment of each frame is labeled with a corresponding number in (a). The cross in the center of each frame indicates the center of the particle determined by the processing algorithm, including its error bars.

activated. Here, fourteen events are registered, preferentially distributed along the mirror movement. However, the greater dispersion is not compensated for by this small number of events. Thus, the uncertainty in position is significant. Lastly, frame 3 corresponds to one of the periodic maxima of the signal after modulation was activated, where 300 events were registered with a dispersion similar to that of frame 2, but the increased number of events resulted in smaller spatial uncertainty.

4.2 Measured trajectories using the proposed method

Figure 4.2.1 displays the $x(t)$ and $y(t)$ coordinates, obtained from the same recording used in Fig. 4.1.1, but showing a longer acquisition time. Instead of directly observing the events, the data was processed and converted into positions over time (see 3.4). Since a camera sensor is used, spatial resolution is based on pixels. To convert to real-world spatial units, the pixel size is determined by calibrating the system using a test target (see 3.2). Once calibration is completed, a maximum absolute z-score value is applied, and any data exceeding this threshold is excluded. Figure 4.2.1C shows a reconstruction of the displacement caused by the mirror, illustrating the movement superimposed on the original Brownian motion.

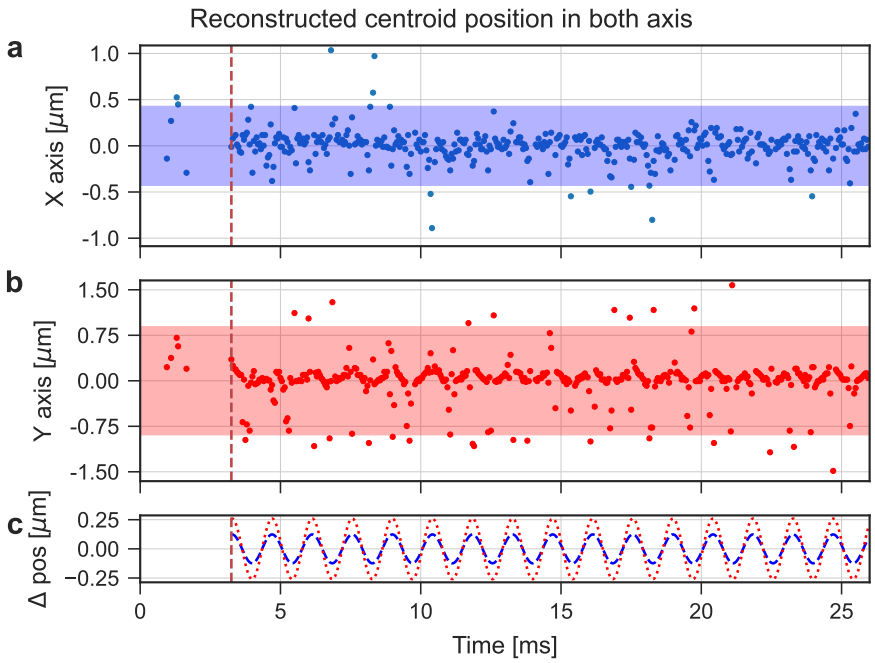

Figure 4.2.1: Measured 2D trajectory of a single Brownian particle. The same dataset as in Figure 4.1.1 was used. (a) and (b) show the coordinates $x(t)$ and $y(t)$ versus time, with each point obtained from events recorded within a $50\mu s$ time window. A z-score filter with a threshold of 2.5 is applied to eliminate outliers prior to analysis, and the colored region illustrates the points that pass the filter. (c) Displacement due to mirror movement reconstructed from the number of events and the mean-squared displacement of the particle. The x and y components are represented by blue dashed and red dotted lines, respectively. In all three panels, a red dashed line indicates the instant when modulation begins.

4.3 Validation through diffusion coefficient measurement

Figure 4.3.1 presents the comparison between the diffusion coefficient of the medium derived from the data collected by the EBC and those provided by phenomenological models.

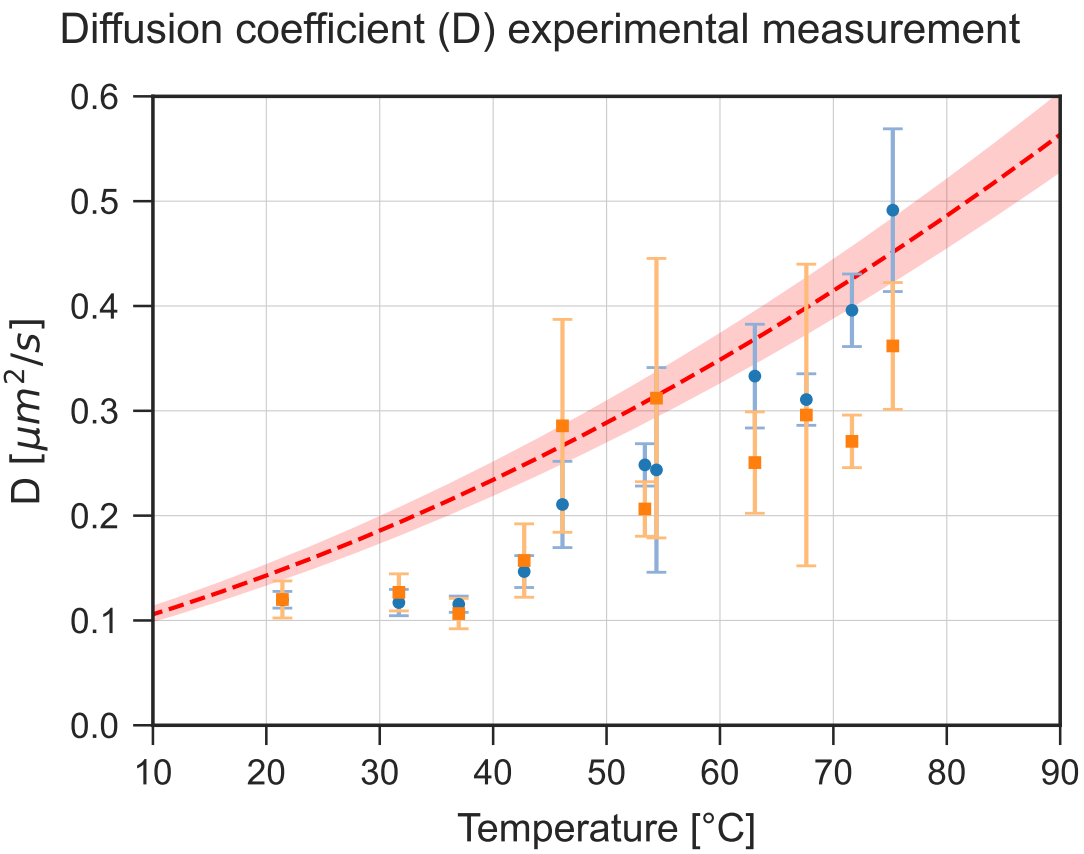

Figure 4.3.1: Diffusion coefficient of the medium as a function of sample temperature. The values from the phenomenological model are represented by a red dashed line, while the colored confidence region reflects an uncertainty of 0.1 μm in the particle radii. The diffusion coefficient is obtained from the slope of the mean square displacement curve, with the x (blue circles) and y (orange squares) components analyzed separately. Each marker denotes the mean value of D from all 3-second clips within a 4°C temperature bin, and the error bars represent the standard error of the mean.

The data were collected using our experimental setup depicted in Fig. 3.1.1, with a modulation frequency of 1 kHz and for particles with a radius of 1.5μm. Videos were recorded across a temperature range from 19.4°C (ambient temperature) to

75.6°C. The maximum temperature is constrained by the stability of samples, which we set well below 90°C at which point extreme motion takes the microparticle outside the ROI and the integrity of the coverslip sealing is compromised.

The position of the particle was estimated from 50 μs time windows. After converting events into positions, frequency filters were applied before cutting each recording into 3-second clips. Then, the MSD of the particles is calculated over a series of time intervals (τ) for each clip, and the diffusion coefficient D is extracted from linear fits to Eq. (2.2.3). This process results in around 650 different estimates for D. To convert them into a statistically more reliable result, we grouped the measurements into 4°C bins and show their mean value and standard error of the mean in Fig. 4.3.1.

The expected values obtained from the literature are shown in Fig 4.3.1 as a dashed line, representing theoretical estimates of the diffusion coefficient calculated using the Stokes-Einstein-Sutherland equation and the temperature dependence of the viscosity of water for a microsphere with a radius of 1.5 mum. The shaded region indicates the confidence band of $D(T)$, accounting for a particle radius uncertainty range between 1.4 μm and 1.6 μm.

4.4 Validation through entropy and complexity analysis

To analyze the behavior of the particles in the PE-SC space, we used the same data employed for the MSD analysis without frequency filtering. The data was divided into 3-second clips, and the PE and SC were calculated for each clip using an embedding dimension $m = 6$ and an embedding delay $\tau_{PE} = 1$. Note that a 3-second clip with an acquisition time of 50 μm comprises 60000 points, satisfying the criteria for a robust PE estimation.

Figure 4.4.1 shows the distribution of clips in a complexity-entropy plane using a color map. This figure also compares PE and SC values for known processes, including fractal Brownian motion (fBm) calculations at different Hurst exponents, H, and sinusoidal functions with different frequencies. While not shown explicitly, it is important to highlight that a more thorough analysis of the PE and SE indicates minimal variation in their values when the amplitude and phase of the

sinusoidal signal change.

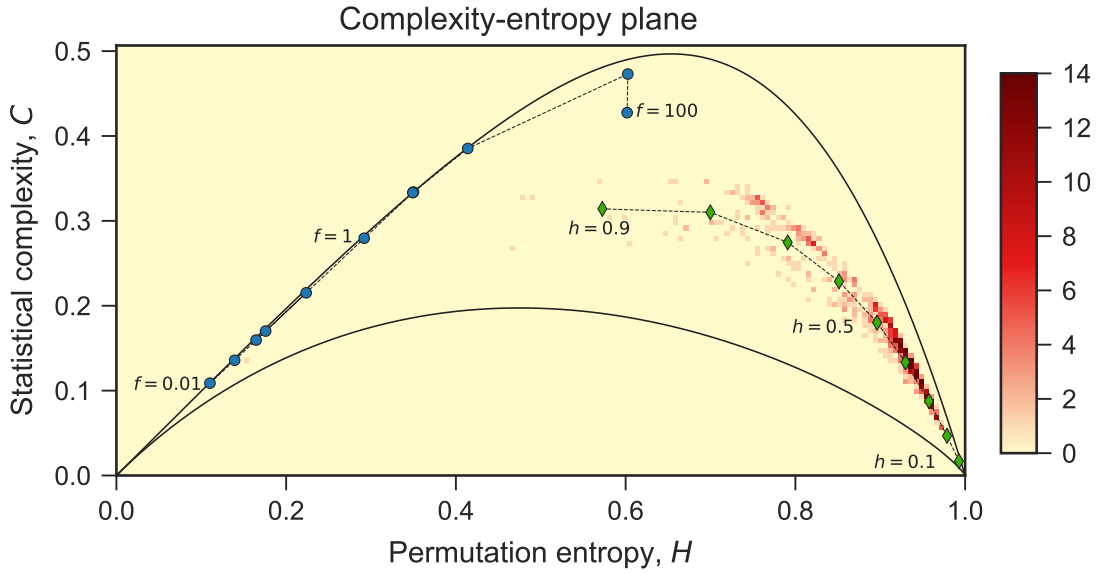

Figure 4.4.1: Complexity-entropy plane for measured trajectories. Permutation entropy (PE) and statistical complexity (SC) are calculated for each 3-second clip. The color map represents the distribution of the clips in the complexity-entropy plane, with darker colors indicating a higher density of clips within that region. Due to the relationship between PE and SC, only the region inside the solid lines is accessible. For reference, the PE and SC values for fractal Brownian motion (fBm) with varying Hurst exponents (green diamonds) and sinusoidal functions with different frequencies (blue circles) are shown. The experimental data points cluster in the region of Brownian processes, suggesting statistical complexity akin to Brownian motion for the measured trajectories.

The results indicate that the data points are distributed near the fBm curve, suggesting a statistical complexity similar to Brownian motion for the measured trajectories. Deviations from the expected values may be due to various factors, including noise in the position measurement and the interaction between the particle and the aqueous medium, which generates a motion not purely Brownian.

Furthermore, there is a clear distinction between the regions of sinusoidal and Brownian motion in the complexity-entropy plane, with experimental data predominantly located in the Brownian processes region. This detection method and data analysis enable us to conclude that the proposed method effectively captures the Brownian behavior of the particles.

Chapter 5

Final remarks

This research aimed to develop and validate a novel methodology to enhance the performance of event-based cameras in microscopy applications, with particular focus on microparticle tracking. Through systematic investigation and experimentation, we have successfully demonstrated that controlled optical modulation can significantly increase event stream density while preserving the underlying stochastic nature of the observed phenomena.

As for the specific objectives outlined in Chapter 1, we have achieved the following:

The first objective was to implement an experimental setup capable of introducing controlled relative motion between the camera and image plane. We successfully achieved this through a piezoelectric-controlled steering mirror system that modulates light before it reaches the event-based camera sensor.

For our second objective, we developed robust algorithms to convert the enhanced event stream into accurate particle trajectories. This algorithm takes advantage of the format in which EBCs register the information without having to rely on converting events into frames to then be processed using traditional tracking algorithms.

The third objective was to validate our approach, which was achieved by two complementary approaches. One consisted of comparing the measured diffusion coefficient of microparticles to theoretical predictions, and the other, in analyzing the permutation entropy and statistical complexity of the particle trajectories. From both of them, we conclude that the optical modulation technique does

preserve the stochastic nature of the Brownian motion. Nonetheless, separating the effect of the modulation from the actual motion of the particles is a challenging task.

Beyond Brownian motion tracking with bright-field configurations, our method is highly adaptable to a wide range of microscopy systems and sample types. This versatility stems from the enhanced sensitivity of event-based sensors to a broad spectrum of light intensities and frequencies, as well as their efficient memory usage compared to conventional imaging techniques. These characteristics make event-based cameras particularly suitable for applications where high-speed, high-contrast detection is crucial, even under low-light conditions or when working with weakly scattering samples.

Additionally, because optical modulation is applied externally and does not alter the sample itself, this approach is especially advantageous for studying delicate biological and soft-matter systems that might be affected by invasive measurement techniques. One promising application is in the study of microbubble solutions used in contrast-enhanced ultrasound imaging and ecotomography. Microbubbles are used as contrast agents due to their strong acoustic response, but their precise behavior and interactions remain challenging to capture with conventional imaging methods. Due to the high temporal resolution and sensitivity of event-based sensors, our technique could improve real-time tracking of individual microbubbles, offering new insights into their behavior that could improve imaging techniques reliant on them.

Despite its advantages, the method still presents challenges that open paths for future research. One of the main difficulties, and a central aspect of this work, is isolating the contribution of optical modulation from the actual motion of the tracked objects. Improving this aspect would enable the use of several standard techniques to analyze the measured trajectories. Additionally, advancements in event-processing algorithms could enhance tracking accuracy, particularly in high-density particle environments that currently exceed the capabilities of our technique. Finally, exploring alternative modulation techniques or optimizing the frequency and amplitude of the introduced motion may lead to more efficient implementations and further enhancements in spatial and temporal resolution.

In summary, we have successfully developed a cost-effective, artifact-free method

for controllably increasing the stream of events in an event-based camera, enhancing both temporal and spatial resolution for microparticle tracking. The proposed technique enables us to study the dynamics of stochastic processes at the microscale without altering their stochastic nature. Our results highlight that neuromorphic-based camera technology can provide exceptional precision in microscopy, particularly for microparticle tracking. This advancement paves the way for innovative research in various fields where precise tracking or calibration of microparticles exhibiting Brownian motion is essential, while also highlighting the pending challenges in the technique.

References

[1] F. A. Merchant and K. R. Castleman, eds., *Microscope image processing*, Second edition (Academic Press, an imprint of Elsevier, London, United Kingdom ; San Diego, CA, 2023).

[2] H. Wang, L. Hong, and L. P. Chamorro, "Micro-Scale Particle Tracking: From Conventional to Data-Driven Methods", Micromachines **15**, Number: 5 Publisher: Multidisciplinary Digital Publishing Institute, 629 (2024).

[3] J. P. Staforelli, E. Vera, J. M. Brito, et al., "Superresolution imaging in optical tweezers using high-speed cameras", Optics Express **18**, Publisher: Optica Publishing Group, 3322–3331 (2010).

[4] M. A. Mahowald and C. Mead, "The Silicon Retina", Scientific American **264**, Publisher: Scientific American, a division of Nature America, Inc., 76–83 (1991).

[5] G. Gallego, T. Delbrück, G. Orchard, et al., "Event-Based Vision: A Survey", IEEE Transactions on Pattern Analysis and Machine Intelligence **44**, Conference Name: IEEE Transactions on Pattern Analysis and Machine Intelligence, 154–180 (2022).

[6] D. Drazen, P. Lichtsteiner, P. Häfliger, et al., "Toward real-time particle tracking using an event-based dynamic vision sensor", Experiments in Fluids **51**, 1465–1469 (2011).

[7] Z. Ni, C. Pacoret, R. Benosman, et al., "Asynchronous event-based high speed vision for microparticle tracking", Journal of Microscopy **245**, 236–244 (2012).

[8] J. Howell, T. C. Hammarton, Y. Altmann, et al., "High-speed particle detection and tracking in microfluidic devices using event-based sensing", Lab on a Chip **20**, Publisher: The Royal Society of Chemistry, 3024–3035 (2020).

[9] C. E. Willert and J. Klinner, "Event-based imaging velocimetry: an assessment of event-based cameras for the measurement of fluid flows", Experiments in Fluids **63**, 101 (2022).

[10] Y. Wang, R. Idoughi, and W. Heidrich, "Stereo Event-Based Particle Tracking Velocimetry for 3D Fluid Flow Reconstruction", in *Computer Vision – ECCV 2020*, Vol. 12374, edited by A. Vedaldi, H. Bischof, T. Brox, et al., Series Title: Lecture Notes in Computer Science (Springer International Publishing, Cham, 2020), pp. 36–53.

[11] C. Cabriel, T. Monfort, C. G. Specht, et al., "Event-based vision sensor for fast and dense single-molecule localization microscopy", Nature Photonics **17**, Publisher: Nature Publishing Group, 1105–1113 (2023).

[12] J. Basumatary, S. Aravinth, N. Pant, et al., "Event-based Single Molecule Localization Microscopy (eventSMLM) for High Spatio-Temporal Super-resolution Imaging", 10.1101/2023.12.30.573392 (2024).

[13] Y. Ren, E. Benedetto, H. Borrill, et al., "Event-based imaging of levitated microparticles", Applied Physics Letters **121**, 113506 (2022).

[14] Y. Auad, M. Walls, J.-D. Blazit, et al., "Event-based hyperspectral EELS: towards nanosecond temporal resolution", Ultramicroscopy **239**, 113539 (2022).

[15] R. Mangalwedhekar, N. Singh, C. S. Thakur, et al., "Achieving nanoscale precision using neuromorphic localization microscopy", Nature Nanotechnology **18**, 380–389 (2023).

[16] Z. Ge, Y. Gao, H. K.-H. So, et al., "Event-based laser speckle correlation for micro motion estimation", Optics Letters **46**, Publisher: Optica Publishing Group, 3885–3888 (2021).

[17] H. R. Vutukuri, M. Lisicki, E. Lauga, et al., "Light-switchable propulsion of active particles with reversible interactions", Nature Communications **11**, Publisher: Nature Publishing Group, 2628 (2020).

[18] C. Posch, T. Serrano-Gotarredona, B. Linares-Barranco, et al., "Retinomorphic Event-Based Vision Sensors: Bioinspired Cameras With Spiking Output", Proceedings of the IEEE **102**, 1470–1484 (2014).

[19] P. Lichtsteiner, C. Posch, and T. Delbruck, "A 128 × 128 120 dB 15 μs Latency Asynchronous Temporal Contrast Vision Sensor", IEEE Journal of Solid-State Circuits **43**, 566–576 (2008).

[20] R. Brown, "XXVII. *A brief account of microscopical observations made in the months of June, July and August* 1827, *on the particles contained in the pollen of plants; and on the general existence of active molecules in organic and inorganic bodies*", The Philosophical Magazine **4**, 161–173 (1828).

[21] A. Einstein, "Über die von der molekularkinetischen Theorie der Wärme geforderte Bewegung von in ruhenden Flüssigkeiten suspendierten Teilchen", Annalen der Physik **322**, _eprint: https://onlinelibrary.wiley.com/doi/pdf/10.1002/andp.19053220806, 549–560 (1905).

[22] W. Sutherland, "LXXV. *A dynamical theory of diffusion for non-electrolytes and the molecular mass of albumin*", The London, Edinburgh, and Dublin Philosophical Magazine and Journal of Science **9**, 781–785 (1905).

[23] X. Michalet, "Mean Square Displacement Analysis of Single-Particle Trajectories with Localization Error: Brownian Motion in Isotropic Medium", Physical review. E, Statistical, nonlinear, and soft matter physics **82**, 041914 (2010).

[24] R. C. Weast, M. J. Astle, and W. H. Beyer, eds., *CRC handbook of chemistry and physics: a ready-reference book of chemical and physical data*, 69. ed (CRC Press, Boca Raton, Fla, 1988).

[25] R. C. Hardy and R. L. Cottington, "Viscosity of deuterium oxide and water in the range 5 to 125 C", Journal of Research of the National Bureau of Standards **42**, 573 (1949).
[26] I. Swindells, J. R. Coe, and T. B. Godfrey, "Absolute Viscosity of Water at 20° C", Journal of Research of the National Bureau of Standards **48** (1952).
[27] J. Kestin, M. Sokolov, and W. A. Wakeham, "Viscosity of liquid water in the range −8°C to 150°C", Journal of Physical and Chemical Reference Data **7**, 941–948 (1978).
[28] International Association for the Properties of Water and Steam, *Release on the iapws formulation 2008 for the viscosity of ordinary water substance*, tech. rep. IAPWS R12-08, Available at http://www.iapws.org (International Association for the Properties of Water and Steam, Sept. 2008).
[29] M. L. Huber, R. A. Perkins, A. Laesecke, et al., "New International Formulation for the Viscosity of H2O", Journal of Physical and Chemical Reference Data **38**, 101–125 (2009).
[30] S Butterworth, "On the Theory of Filter Amplifiers", Experimental Wireless and the Wireless Engineer **7**, 536–541 (1930).
[31] Geek3, *Filters order 5 comparison*, Licensed under CC BY 4.0, 2016.
[32] Inductiveload, *Butterworth filter orders*, This figure is in the public domain, 2007.
[33] A. A. B. Pessa and H. V. Ribeiro, "Ordpy: A Python package for data analysis with permutation entropy and ordinal network methods", Chaos: An Interdisciplinary Journal of Nonlinear Science **31**, 063110 (2021).
[34] C. Bandt and B. Pompe, "Permutation Entropy: A Natural Complexity Measure for Time Series", Physical Review Letters **88**, 174102 (2002).
[35] L. Zunino, M. Zanin, B. M. Tabak, et al., "Forbidden patterns, permutation entropy and stock market inefficiency", Physica A: Statistical Mechanics and its Applications **388**, 2854–2864 (2009).
[36] N. Nicolaou and J. Georgiou, "Detection of epileptic electroencephalogram based on Permutation Entropy and Support Vector Machines", Expert Systems with Applications **39**, 202–209 (2012).
[37] J. Garland, T. R. Jones, M. Neuder, et al., "Anomaly Detection in Paleoclimate Records Using Permutation Entropy", Entropy **20**, 931 (2018).
[38] M. Zanin, L. Zunino, O. A. Rosso, et al., "Permutation Entropy and Its Main Biomedical and Econophysics Applications: A Review", Entropy **14**, 1553–1577 (2012).
[39] J. M. Amigó, K. Keller, and V. A. Unakafova, "Ordinal symbolic analysis and its application to biomedical recordings", Philosophical Transactions of the Royal Society A: Mathematical, Physical and Engineering Sciences **373**, 20140091 (2015).
[40] U. Parlitz, S. Berg, S. Luther, et al., "Classifying cardiac biosignals using ordinal pattern statistics and symbolic dynamics", Computers in Biology and Medicine, Computing complexity in cardiovascular oscillations **42**, 319–327 (2012).

[41] D. Cuesta-Frau, J. P. Murillo-Escobar, D. A. Orrego, et al., "Embedded Dimension and Time Series Length. Practical Influence on Permutation Entropy and Its Applications", Entropy **21**, 385 (2019).

[42] M. Riedl, A. Müller, and N. Wessel, "Practical considerations of permutation entropy", The European Physical Journal Special Topics **222**, 249–262 (2013).

[43] O. A. Rosso, H. A. Larrondo, M. T. Martin, et al., "Distinguishing Noise from Chaos", Physical Review Letters **99**, Publisher: American Physical Society, 154102 (2007).

[44] R. López-Ruiz, H. L. Mancini, and X. Calbet, "A statistical measure of complexity", Physics Letters A **209**, 321–326 (1995).

[45] M. Zanin and F. Olivares, "Ordinal patterns-based methodologies for distinguishing chaos from noise in discrete time series", Communications Physics **4**, Publisher: Nature Publishing Group, 1–14 (2021).

[46] O. A. Rosso, L. Zunino, D. G. Pérez, et al., "Extracting features of Gaussian self-similar stochastic processes via the Bandt-Pompe approach", Physical Review E **76**, Publisher: American Physical Society, 061114 (2007).

[47] L. Zunino, D. G. Pérez, M. T. Martín, et al., "Permutation entropy of fractional Brownian motion and fractional Gaussian noise", Physics Letters A **372**, 4768–4774 (2008).

[48] L. Kushner, B. Duncan, and J. Hoffman, "A viscometric study of the micelles of sodium dodecyl sulfate in dilute solutions", Journal of Research of the National Bureau of Standards **49**, 85 (1952).

[49] H. Qian, M. P. Sheetz, and E. L. Elson, "Single particle tracking. Analysis of diffusion and flow in two-dimensional systems", Biophysical Journal **60**, 910–921 (1991).

[50] J. G. Proakis and D. G. Manolakis, *Digital signal processing: principles, algorithms, and applications*, 4. ed (Pearson/Prentice Hall, Upper Saddle River, NJ, 2007).